

AnomalyNCD: Towards Novel Anomaly Class Discovery in Industrial Scenarios

Ziming Huang^{1,*} Xurui Li^{1,*} Haotian Liu^{1,*} Feng Xue⁴ Yuzhe Wang¹ Yu Zhou^{1,2,3,†}

¹School of Electronic Information and Communications, Huazhong University of Science and Technology

²Hubei Key Laboratory of Smart Internet Technology, Huazhong University of Science and Technology

³Artificial Intelligence Research Institute, Wuhan JingCe Electronic Group Co., LTD

⁴Department of Information Engineering and Computer Science, University of Trento

Abstract

Recently, multi-class anomaly classification has garnered increasing attention. Previous methods directly cluster anomalies but often struggle due to the lack of anomaly-prior knowledge. Acquiring this knowledge faces two issues: the non-prominent and weak-semantics anomalies. In this paper, we propose AnomalyNCD, a multi-class anomaly classification network compatible with different anomaly detection methods. To address the non-prominence of anomalies, we design main element binarization (MEBin) to obtain anomaly-centered images, ensuring anomalies are learned while avoiding the impact of incorrect detections. Next, to learn anomalies with weak semantics, we design mask-guided representation learning, which focuses on isolated anomalies guided by masks and reduces confusion from erroneous inputs through corrected pseudo labels. Finally, to enable flexible classification at both region and image levels, we develop a region merging strategy that determines the overall image category based on the classified anomaly regions. Our method outperforms the state-of-the-art works on the MVTec AD and MTD datasets. Compared with the current methods, AnomalyNCD combined with zero-shot anomaly detection method achieves a 10.8% F_1 gain, 8.8% NMI gain, and 9.5% ARI gain on MVTec AD, and 12.8% F_1 gain, 5.7% NMI gain, and 10.8% ARI gain on MTD. Code is available at <https://github.com/HUST-SLOW/AnomalyNCD>.

1. Introduction

In recent years, industrial anomaly detection [22, 24, 31, 53] has garnered remarkable performance. It locates visual anomalies on industrial products but without recognizing fine-grained anomaly categories. For downstream anomaly treatments, it is necessary to recognize the anomaly classes, such as fracture, ablation, etc., and even discover novel

anomaly categories that are constantly emerging.

Several anomaly clustering approaches [1, 28, 40] have been proposed to address the multi-class anomaly classification task, as illustrated in Fig. 1 (a). These approaches typically employ a two-step process: anomaly localization followed by feature extraction from the anomalous regions for clustering. However, the effectiveness of these methods is limited when dealing with homogeneous anomaly patterns that exhibit differences in shape, appearance, and location, primarily due to the lack of prior knowledge of anomaly types. Therefore, our study aims to classify unseen anomalies by leveraging prior knowledge of seen anomalies, thereby overcoming the limitations of current methods.

Through detailed investigation, we find two primary obstacles in leveraging prior knowledge of known anomalies, which prevent existing classification network to industrial anomalies. **① Non-prominence Anomalies:** Classification in natural scenes assumes that subjects are centered in the images so that networks easily extract their semantics, while this assumption is not true in industrial scenarios. **② Low-semantics Anomalies:** In contrast to natural objects, industrial anomalies are typically less semantic, making the network hard to focus on anomalies but prone to background.

In this paper, we overcome both obstructions and propose a multi-class anomaly classification network that aligns with the concept of novel class discovery (NCD), as illustrated in 1 (c). This network learns to classify isolated anomalies by focusing the model’s attention on real anomaly regions. Firstly, to address the non-prominence issue, we propose a main element binarization (MEBin) method. MEBin isolates the primary anomaly regions by extracting them from anomaly detection (AD) results. This binarization process alleviates the negative impact of errors within AD results on the subsequent multi-class anomaly learning, enabling compatibility with various AD algorithms. Secondly, to tackle low-semantics anomalies, we propose mask-guided representation learning. It leverages the anomaly masks generated by MEBin to direct the network’s attention specifically to individual anomalous re-

* Contributed Equally. † Corresponding Author.

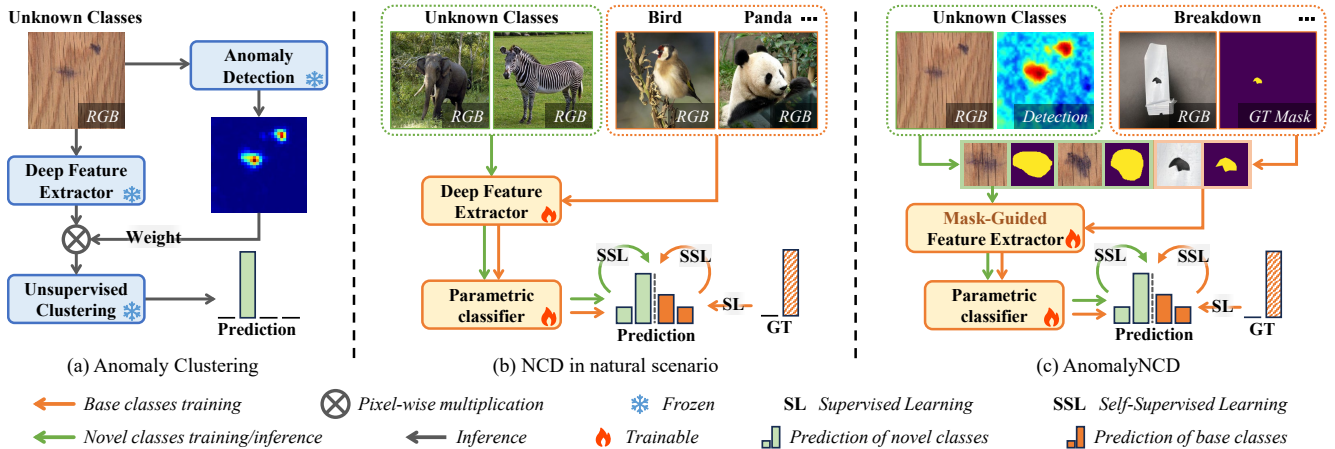


Figure 1. **Comparison between solutions organizing anomalies into groups.** (a) Anomaly clustering methods extract the features of the anomaly region and employ unsupervised clustering algorithms to cluster the anomalies. (b) Vanilla NCD methods typically employ a trainable feature extractor and classifier. These components process object-centered images from both known and unknown classes. (c) Our method aims to learn features of isolated anomaly regions using anomaly-centered sub-images and masks from MEBin.

gions, ensuring our network learns more discriminative features specific to anomalies and classifies each individual anomaly. Additionally, we use corrected pseudo labels in this learning method to prevent false-positive anomalies from training. Finally, to achieve more flexible classification in both region and image levels, we propose a region merging strategy, which determines the image category according to the classification of each region in the image. Experimental results on the MVTec AD [5] and MTD datasets [23] demonstrate the effectiveness of AnomalyNCD.

In summary, the major contributions of our work are:

- We propose the first method based on self-supervised manner in multi-class anomaly classification, named AnomalyNCD. It can be seamlessly combined with different anomaly detection methods and classify unseen anomalies detected into homogeneous groups.
- We study the challenges of learning from anomalous regions in industrial scenarios, motivating us to propose MEBin and mask-guided representation learning for our network to focus on real anomalous regions and learn discriminative features of isolated anomalies.
- AnomalyNCD surpasses existing anomaly clustering methods and NCD methods on the MVTec AD and MTD datasets, providing a decent foundation for downstream anomaly treatments in industrial scenarios.

2. Related Work

2.1. Image Clustering in Industrial Scenarios

Directly clustering the images cannot perform well in multi-class anomaly classification. To address this issue, two studies build the clustering pipeline specific for fine-grained anomaly classes. Sohn *et al.* [40] proposed a simple but effective method to aggregate the patch features by anomaly map weighting. Lee *et al.* [28] only aggregates the patch

features with the higher anomaly score to determine the classes. However, both methods rely on frozen models that cannot learn features specific to anomalies. Therefore, we adopt self-supervised learning to discover novel classes from unlabeled anomalies.

2.2. Novel Class Discovery

Novel Class Discovery setting was first formalized in [18]. The early methods follow a two-stage pipeline [18, 20, 21]. The first stage is to learn representation from the base set to obtain prior knowledge for classification, which serves as the basis for the second one to train the model on the novel set. Recent methods are one-stage [19, 46, 56]. By handling the base set and novel set simultaneously, one-stage methods extract better representations with less bias towards the base classes. NCD has been applied in several fields, such as medical image classification [14, 58], semantic segmentation [55] and point cloud segmentation [37, 49]. In this paper, we introduce the NCD architecture into multi-class industrial anomaly classification for the first time.

2.3. Binarization Approach

Binarization is a crucial preprocessing step for various vision tasks, e.g., edge detection [6, 59], segmentation [10, 16, 57], document image processing [7, 34, 41], medical image processing [39, 42], object detection [50–52], etc. Otsu [35] determines the optimal threshold to separate the foreground and background by maximizing the between-class variance of the pixel intensities. DiffuMask [48] utilizes cross-attention maps and adaptive thresholding to generate binary maps. However, these methods usually obtain fragmented false-positive regions when segmenting the anomalies, which harms the region-level anomaly class prediction. To alleviate this, we propose the main element

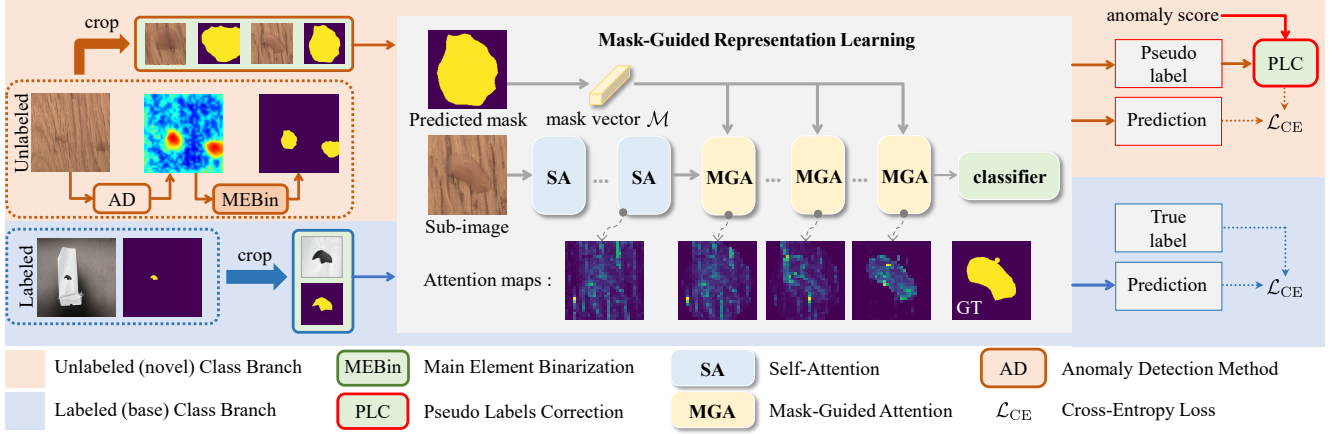


Figure 2. **Illustration of the Training Process for AnomalyNCD.** First, we apply main element binarization (MEBin) to segment anomaly masks from detection results and generate anomaly-centered sub-images. Second, we introduce mask-guided representation learning to learn discriminative features of anomalies, classifying sub-images into various categories.

binarization strategy to extract only the primary anomaly region, thereby reducing the impact of false positives on representation learning.

3. Method

The proposed AnomalyNCD aims to automatically discover and recognize the visual categories of industrial anomalies. Fig. 2 illustrates its overall framework. To extract main anomaly regions from detection results, we outline the main element binarization method (Sec. 3.2). Guided by these anomaly regions, we then apply mask-guided representation learning (Sec. 3.3) to extract and classify discriminative features of anomalies within these regions. Finally, a region merging strategy (Sec. 3.4) ensures robust image-level classification based on all anomaly regions.

3.1. Problem Definition

Given a set of unlabelled images $\mathcal{D}^u = \{I_i^u | i \in [1, N^u]\}$, the goal of AnomalyNCD is to assign them into \mathcal{C}^u classes (named “**Novel**” previously), where \mathcal{C}^u is known a priori, referring to vanilla NCD [15, 17, 45]. To provide a better foundation for learning novel classes, we follow previous NCD tasks to assume a set of labeled anomaly images $\mathcal{D}^l = \{(I_i^l, y_i^l, \mathbf{M}_i^l) | i \in [1, N^l]\}$ with \mathcal{C}^l classes available (named “**Base**” previously), where $y_i^l \in \mathbb{R}^{1 \times (\mathcal{C}^l + \mathcal{C}^u)}$ is the one-hot class label, and \mathbf{M}_i^l is the ground truth anomaly mask of image $I_i^l \in \mathcal{D}^l$. \mathcal{D}^l supplies the auxiliary knowledge of the industrial anomalies for grouping the images in \mathcal{D}^u . To further generalize our study, we also perform experiments with different \mathcal{D}^l and without \mathcal{D}^l in the Appendix F.

3.2. Main Element Binarization

To provide a clear anomaly indication of unlabeled images, we use an anomaly detection method on I_i^u to generate the anomaly probability map, denoted as $A_i \in$

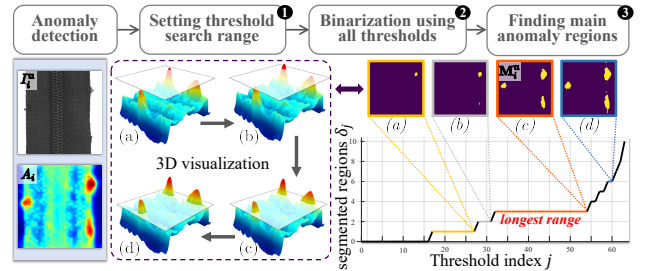


Figure 3. **Pipeline of the Main Element Binarization.** In 3D visualization, we show the changes of segmented regions under different thresholds. The 3D map (a) corresponds to the 2D binary segmentation mask (a).

$[0, 1]^{H \times W}$. However, A_i inevitably contains false positives (over-detections) and false negatives (missed detections). These errors can negatively affect multi-class anomaly classification. To address this, we propose a Main Element Binarization (MEBin) approach. It extracts the principal anomaly structures (Main Element) from A_i by focusing on stable regions across small threshold variations. Overall, the MEBin consists of three steps: **1** Predefine a range $[s_{\min}, s_{\max}]$ for threshold exploration; **2** Binarize A_i across all thresholds within this range; **3** Identify the main elements in A_i based on the changes of segmented regions under different binarization results.

The first step: To capture all potential anomalies across the set $\{A_i | i \in [1, N^u]\}$, the upper limit s_{\max} is set to 1. Conversely, the lower limit, s_{\min} , is determined by the minimum anomaly score¹ found across the set $\{A_i | i \in [1, N^u]\}$, represented as $s_{\min} = \min(s_1, s_2, \dots, s_{N^u})$, where $s_i = \max(A_i)$. Such a lower limit helps minimize the likelihood of normal image pixels being segmented.

The second step: To analyze the segmented regions

¹Anomaly score: Maximum value in an anomaly probability map.

change with thresholds, we uniformly sample \mathcal{T} thresholds $\{\epsilon_j | j \in [1, \mathcal{T}]\}$ in $[\mathbf{s}_{\min}, \mathbf{s}_{\max}]$. For each threshold ϵ_j , the anomaly map A_i is binarized into a mask M_i^j : $M_i^j = \mathbb{1}[A_i > \epsilon_j]$, where $\mathbb{1}[\cdot]$ is the indicator function. To reduce the meaningless and fragmented segmentation, we further apply the erosion operation to each mask M_i^j .

The third step: We identify main anomaly regions through two operations. First, let δ_i^j denote the number of individual regions segmented in M_i^j , each region is an independent connected component. We observe that the amount of the main regions in the anomaly map A_i can be characterized by the non-zero value that appears most frequently in $\{\delta_i^j | j \in [1, \mathcal{T}]\}$, denoted as $\bar{\delta}_i$. Second, to segment the main regions, we take the longest continuous threshold range where only $\bar{\delta}_i$ regions are segmented. The main anomaly regions remain stable within this threshold range, as shown in Fig. 3.

- If this range is shorter than τ , there is no anomaly region to be segmented.
- Conversely, if this range exceeds τ , it confirms stable anomaly segmentation within this threshold range. In this case, we select the minimum threshold from the identified range to segment anomalies as completely as possible.

Finally, we use the selected threshold to segment A_i into the binary mask, denoted as M_i^u . In this way, the unlabeled images set \mathcal{D}^u are extended with the binary masks: $\{(I_i^u, M_i^u) | i \in [1, N^u]\}$.

Anomaly-Centered Sub-Image Cropping. To focus the model on anomalous regions, we crop each region in M_i^u individually into anomaly-centered sub-images. Specifically, for each region in M_i^u , we use the minimum bounding square to crop the sub-image from I_i^u and its mask from M_i^u . Then the sub-images of I_i^u can be denoted as $\{x_{i,1}^u, x_{i,2}^u, \dots\}$, and the corresponding masks cropped from M_i^u are denoted as $\{m_{i,1}^u, m_{i,2}^u, \dots\}$. To align labeled and unlabeled inputs, we use the same cropping operation to extract sub-images and masks for the labeled data set \mathcal{D}^l , denoted as $\{(x_{i,1}^l, m_{i,1}^l), (x_{i,2}^l, m_{i,2}^l), \dots | i \in [1, N^l]\}$. These are then merged with the unlabeled data in the same structures, represented as $\{(x_{i,k}, m_{i,k}, y_{i,k}) | i \in [1, N^l + N^u], k \in [1, \bar{\delta}_i]\}$, where $\bar{\delta}_i$ indicates the number of sub-images per image, and $y_{i,k}$ is the one-hot class label for each labeled sub-image, matching the label of the i^{th} image if it belongs to \mathcal{D}^l . Implementation details of the cropping process are supplied in the Appendix C.

3.3. Mask-Guided Representation Learning

3.3.1. Mask-Guided Vision Transformer (MGViT)

MGViT is built on vision transformer (ViT). Thus we review its structure.

Vision transformer [13] processes an input image by dividing it into N fixed-size patches. Each patch is treated as a

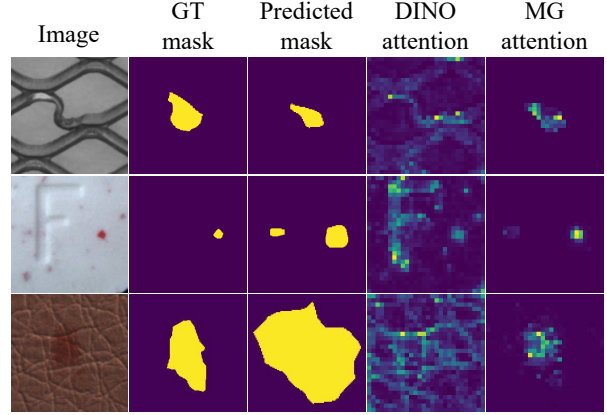


Figure 4. **Visualization of the self-attention of the [CLS] token on the last layer’s heads.** DINO attention refers to the [CLS] token extracted from a DINO pre-trained ViT that mainly focuses on a foreground object. AnomalyNCD uses a mask to direct the [CLS] token’s attention to the anomalous regions.

“token” and is flattened into an embedding vector of length D . ViT has L sequential transformer layers, each containing self-attention layers and feed-forward neural networks. In addition, a special class token [CLS], is propagated from the first layer to the final layer where it serves as the basis for classification. In the self-attention of the l^{th} layer, the input patches undergo linear projections to form the queries, keys, and values $\mathbf{Q}_{l-1}, \mathbf{K}_{l-1}, \mathbf{V}_{l-1} \in \mathbb{R}^{(N+1) \times D}$. Here, ViT captures the relationships between the image patches by self-attention mechanism $Attn$ as follows:

$$Attn = \text{softmax}(\text{concat}(\mathbf{Q}_{l-1}^{\text{cls}} \mathbf{K}_{l-1}^{\text{T}}, \mathbf{Q}_{l-1}^{\text{patch}} \mathbf{K}_{l-1}^{\text{T}})) \mathbf{V}_{l-1} \quad (1)$$

where we divide \mathbf{Q}_{l-1} into $\mathbf{Q}_{l-1}^{\text{cls}} \in \mathbb{R}^{1 \times D}$ and $\mathbf{Q}_{l-1}^{\text{patch}} \in \mathbb{R}^{N \times D}$ to represent class token and patch tokens separately.

Insufficient Focus on Anomalies. The ViT excels in semantic representation but fails to detect weak semantic anomalies. Fig. 4 demonstrates this using the self-attention map of the [CLS] token in the last layer of a DINO-pretrained ViT [9]. In the 1st row’s example, the model highlights the salient object (metal grid) in an image, rather than the local anomaly. This observation means that the network over-focuses on learning background.

Mask-Guided Attention. To address the issue above, we propose mask-guided attention to direct ViT’s focus on the anomalous region. Specifically, the input sub-image $x_{i,k}$ is fed into the ViT, and we assume the token number is N . At the same time, its mask $m_{i,k}$ is resized to $\sqrt{N} \times \sqrt{N}$ by average pooling and then flattened into a vector $\mathcal{M} \in \mathbb{R}^{N \times 1}$. Subsequently, we insert the constant 1 at the beginning of \mathcal{M} to align its size with the tokens. Next, we use the mask vector in the self-attention mechanism for re-directing focus, which has three possible design choices.

1. Adding the mask \mathcal{M} on both class and patch tokens.
2. Adding the mask \mathcal{M} on the patch tokens.

3. Adding the mask \mathcal{M} on the class token.

The 1st and 2nd designs suppress the rich contextual features in patch tokens that are crucial for classification, and our network only focuses on classifying anomalies rather than segmenting. Thus, the 3rd one is recommended as the most suitable design, and the experiment also verifies its effectiveness. Such a design can be formulated as follows:

$$\text{Attn} = \text{softmax}(\text{concat}(\mathbf{Q}_{l-1}^{\text{cls}} \mathbf{K}_{l-1}^{\top} + \overline{\mathcal{M}}, \mathbf{Q}_{l-1}^{\text{patch}} \mathbf{K}_{l-1}^{\top})) \mathbf{V}_{l-1} \quad (2)$$

where $\overline{\mathcal{M}}$ denotes the converted mask vector that is compatible with the attention mechanism [12]:

$$\overline{\mathcal{M}}(i) = \begin{cases} 0, & \text{if } \mathcal{M}(i) > 0.5 \\ -\infty, & \text{otherwise} \end{cases} \quad (3)$$

Note that, in the ViT, the self-attention in the last L_m -layer is replaced with the mask-guided attention to form MGViT. Fig. 4 reveals that the [CLS] token focuses on anomalous regions by using our mask-guided attention. Even though the predicted masks do not align with the ground truth accurately, the network still focuses on the anomaly roughly.

3.3.2. Model Training

Given a sub-image pair $(x_{i,k}, m_{i,k})$, we first apply random augmentation to generate two views $(\tilde{x}_{i,k}, \tilde{m}_{i,k})$ and $(\hat{x}_{i,k}, \hat{m}_{i,k})$. Following DINO [9], we feed these two views into the teacher and student networks respectively, which have shared MGViT and classification heads with different softmax temperatures. For labeled sub-images, the ground truth labels are converted into one-hot vectors to serve as supervision targets for the student network. For unlabeled sub-images $\tilde{x}_{i,k}, \hat{x}_{i,k}$, we generate pseudo labels $\hat{q}_{i,k}, \tilde{q}_{i,k} \in \mathbb{R}^{1 \times (C^1 + C^u)}$ by the ‘‘teacher’’ one, which employs a sharp temperature τ_t to produce confident predictions. The entries of labeled classes (C^1) in the pseudo labels are set to 0. The ‘‘student’’ one, using a smooth temperature τ_s , is trained to align its probability predictions $\hat{p}_{i,k}, \tilde{p}_{i,k} \in \mathbb{R}^{1 \times (C^1 + C^u)}$ with either ground truth labels (for labeled data) or pseudo labels (for unlabeled data). This dual supervision ensures effective learning from both labeled and unlabeled data.

Our training objective follows existing category discovery methods [45, 47] and includes classification objective and representation learning objective. The classification objective contains ground truth label supervision $\mathcal{L}_{\text{cls}}^1$ on labeled sub-images, and pseudo label supervision $\mathcal{L}_{\text{cls}}^u$ on unlabeled sub-images. The representation learning objective contains self-supervised contrastive learning \mathcal{L}_{rep} [11] on both labeled sub-images and unlabeled sub-images, and supervised contrastive learning $\mathcal{L}_{\text{rep}}^1$ [26] on only labeled sub-images. Finally, we adopt a mean-entropy maximization regularizer $\mathcal{L}_{\text{reg}}^u$ [8] for unlabeled sub-images. More details about the training procedure are provided in Appendix A.

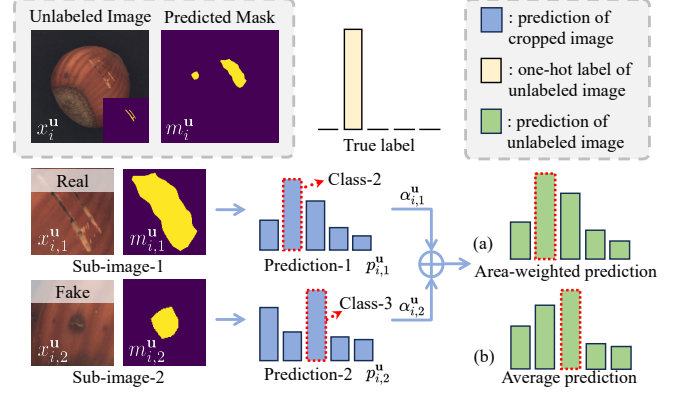


Figure 5. **Region merging strategy for image-level classification.** Using average prediction, the output of normal cropped images (Sub-image-2) leads to final misclassification, while area-weighted prediction can reduce the negative effect of normal cropped images on the final result.

The overall loss of training objective is written as:

$$\mathcal{L} = \lambda(\mathcal{L}_{\text{rep}}^1 + \mathcal{L}_{\text{cls}}^1) + (1 - \lambda)(\mathcal{L}_{\text{rep}} + \mathcal{L}_{\text{cls}}^u + \mu \mathcal{L}_{\text{reg}}^u) \quad (4)$$

where λ is a hyperparameter that balances the supervised loss and the self-supervised loss. μ is the coefficient of the regularization.

Pseudo Labels Correction. The error in pseudo labels leads to the false learning objective for the classification model. To mitigate these errors, especially the false detection of anomalous regions, we propose to use anomaly scores (described in Sec 3.2) to correct pseudo labels.

Let $s_{i,k}$ denote the anomaly score for $x_{i,k}$, we weightedly judge whether the view $\hat{x}_{i,k}$ should be labeled as normal or assigned the generated pseudo labels.

$$\hat{q}_{i,k} \leftarrow w_{i,k} \mathbf{e} + (1 - w_{i,k}) \hat{q}_{i,k}; \quad w_{i,k} = \max(0.5 - s_{i,k}, 0) \quad (5)$$

where $w_{i,k}$ is the weight for normal. $\mathbf{e} \in \mathbb{R}^{1 \times (C^1 + C^u)}$ denotes a unit vector whose $(C^1 + 1)$ -th value is 1 and all other values are 0, in which we use the first class in the C^u classes as normal. If $s_{i,k}$ is smaller, the more likely the sub-image $\hat{x}_{i,k}$ is normal, and $\hat{q}_{i,k}$ is closer to \mathbf{e} . Thus, such correction forces the network to separate normal sub-images from the train set. In the same way, the pseudo label $\tilde{q}_{i,k}$ is updated.

3.4. Region Merging for Image Classification

For flexible classification in both sub-image and image levels, we aim to determine the image’s anomaly class according to its sub-image classification. Intuitively, a naive method is to average the predictions of all sub-images within an image. However, false classification of the over-detected region may mislead the image class. As shown in Fig. 5, *Sub-image-1* and *Sub-image-2* are classified to *Class-2* and *Class-3*, respectively, where the wrong prediction of *Sub-image-2* misleads the image class in Fig. 5 (b).

| Datasets | Metric | IIC[25] | GATCluster[33] | SCAN[44] | UNO[15] | GCD[45] | SimGCD[47] | AMEND[3] | AC[40] (Unsup.) | MuSc [30] +AnomalyNCD |
|--------------|--------|---------|----------------|----------|---------|--------------|------------|----------|--------------------|--------------------------|
| MVTec AD [5] | NMI | 0.093 | 0.136 | 0.210 | 0.146 | 0.417 | 0.452 | 0.431 | <u>0.525</u> | 0.613 |
| | ARI | 0.020 | 0.053 | 0.103 | 0.052 | 0.302 | 0.346 | 0.333 | <u>0.431</u> | 0.526 |
| | F_1 | 0.285 | 0.264 | 0.335 | 0.342 | 0.553 | 0.569 | 0.542 | <u>0.604</u> | 0.712 |
| MTD [23] | NMI | 0.064 | 0.028 | 0.041 | 0.034 | <u>0.211</u> | 0.105 | 0.138 | 0.179 | 0.268 |
| | ARI | 0.020 | 0.009 | 0.029 | 0.011 | 0.115 | 0.048 | 0.067 | <u>0.120</u> | 0.228 |
| | F_1 | 0.252 | 0.243 | 0.282 | 0.221 | <u>0.381</u> | 0.293 | 0.324 | 0.346 | 0.509 |

Table 1. Quantitative results on the MVTec AD and MTD dataset. All the methods only use unlabeled images as input. The best-performing result is in bold, the second best result is underlined.

| Datasets | Metric | AC[40] (Semi-sup.) | UniFormaly[28] (0.953 / 0.837) | PatchCore[38] (0.938 / 0.729) +AnomalyNCD | RD++[43] (0.950 / 0.741) +AnomalyNCD | EfficientAD[4] (0.917 / 0.731) +AnomalyNCD | PNI[2] (0.942 / 0.516) +AnomalyNCD | CPR[29] (0.964 / -) +AnomalyNCD |
|--------------|--------|-----------------------|-----------------------------------|---|--|--|--|---------------------------------------|
| MVTec AD [5] | NMI | 0.608 | 0.547 | 0.670 | 0.631 | 0.516 | <u>0.675</u> | 0.736 |
| | ARI | 0.489 | 0.433 | 0.601 | 0.542 | 0.394 | <u>0.609</u> | 0.674 |
| | F_1 | 0.652 | 0.645 | <u>0.769</u> | 0.721 | 0.641 | <u>0.769</u> | 0.805 |
| MTD [23] | NMI | <u>0.390</u> | 0.421 | 0.380 | 0.368 | 0.220 | 0.181 | - |
| | ARI | 0.314 | 0.322 | 0.390 | <u>0.361</u> | 0.188 | 0.219 | - |
| | F_1 | 0.490 | <u>0.609</u> | 0.617 | 0.600 | 0.467 | 0.465 | - |

Table 2. Quantitative results on the MVTec AD and MTD dataset. All the methods use unlabeled images and labeled normal images as input. We evaluate the AUPRO metric across various anomaly detection approaches on two datasets, e.g., (0.953 / 0.837), the first one on the MVTec AD dataset and the second on the MTD dataset. For the metrics of multi-class anomaly classification, the best-performing result is in bold, the second best result is underlined. The unofficial results are marked in gray .

To address this issue, we propose a region merging approach to robustly classify images. We found that misclassification is mostly over-detected regions that are much smaller than real anomalies. Therefore, we define an area-related weight $\alpha_{i,k}^u$ for each sub-image $x_{i,k}^u$, which is used in determining the image category:

$$\alpha_{i,k}^u = \frac{\exp(\sqrt{\mathbf{a}_{i,k}^u}/\tau_\alpha)}{\sum_{k=1}^{\delta_i} \exp(\sqrt{\mathbf{a}_{i,k}^u}/\tau_\alpha)} \quad (6)$$

where $\mathbf{a}_{i,k}^u$ is the area of anomaly in $x_{i,k}^u$, and τ_α is the temperature value. Then, for an image I_i^u composed by sub-images $\{x_{i,k}^u | k \in [1, \delta_i]\}$, the prediction logit is $p_i^u = \sum_{k=1}^{\delta_i} \alpha_{i,k}^u p_{i,k}^u$, where $p_{i,k}^u$ is the probability prediction of $x_{i,k}^u$ generated by the student network. As shown in Fig. 5 (a), the prediction p_i^u depends more on $p_{i,1}^u$, which has a larger weight $\alpha_{i,1}^u$ and a correct prediction.

4. Experiments

4.1. Experimental setting

4.1.1. Datasets

We conduct experiments on industrial datasets MVTec AD [5] and Magnetic Tile Defect (MTD) [23]. MVTec AD has industrial product images of 10 object categories and 5 texture categories. Each product category has at least two anomaly classes. Following [40] and [28], we remove the combined anomaly classes for a fair comparison. Notice that our method can also handle the combined anomaly

class, as described in the Appendix G. MTD dataset has 952 normal images and 392 abnormal images, the abnormal images are divided into five anomaly classes. We follow [40] that uses 80% of normal images as the reference images and the rest as the test images. For both datasets, we use the single-blade sub-dataset in Aero-engine Blade Anomaly Detection Dataset (AeBAD-S) [54] with the normal class removed, as our default labeled image set \mathcal{D}^l .

4.1.2. Implementation details

We use ViT-B/8 [13] pre-trained with DINO [9] as our feature extractor. The self-attentions in the last 9 layers are replaced with our mask-guided attention. During training, all the layers of ViT are fixed except the last layer. For anomaly detection methods preceding AnomalyNCD, we choose zero-shot method MuSc [30], one-class methods PatchCore [38], EfficientAD [4], RD++ [43], PNI [2] and CPR [29]. More details are in the Appendix B.

4.1.3. Competing methods

We compare our method with two state-of-the-art industrial anomaly clustering methods, UniFormaly [28] and Anomaly Clustering [40] that has two settings: an unsupervised one (Unsup.) and a semi-supervised one (Semi-sup.). The former setting only inputs unlabeled images for clustering, while the latter one uses labeled normal images, same as the input of one-class anomaly detection. We also employ three deep clustering methods, IIC [25], GAT-Cluster [33], and SCAN [44], which cluster unlabeled im-

| | Avg FPR ↓ | Avg FNR ↓ | NMI ↑ | ARI ↑ | F_1 ↑ |
|------------------|--------------|--------------|--------------|--------------|--------------|
| $\epsilon = 0.1$ | 0.572 | 0.617 | 0.554 | 0.482 | 0.650 |
| $\epsilon = 0.3$ | 0.678 | 0.742 | 0.499 | 0.404 | 0.587 |
| $\epsilon = 0.5$ | 0.484 | 0.165 | 0.567 | 0.458 | 0.640 |
| $\epsilon = 0.7$ | 0.269 | 0.247 | 0.495 | 0.395 | 0.623 |
| $\epsilon = 0.9$ | 0.544 | 0.593 | 0.077 | 0.013 | 0.337 |
| Otsu [35] | 0.676 | 0.525 | 0.382 | 0.268 | 0.499 |
| Ours | 0.153 | 0.035 | 0.613 | 0.526 | 0.712 |

Table 3. Ablation study of different binarization approaches on the MVTec AD dataset. The best-performing result is in bold.

ages directly. In addition, four NCD methods in the nature scene are considered for comparison, UNO [15], GCD [45], SimGCD [47] and AMEND [3]. As in our method, the AeBAD-S dataset is used as labeled abnormal images.

4.1.4. Evaluation metrics

We report three widely used metrics for the evaluation of clustering: the F_1 score, the normalized mutual information (NMI) [32], and the adjusted rand index (ARI) [36]. We use the Hungarian algorithm [27] to match the predicted clusters to the ground truth labels. For methods using anomaly maps, we measure the segmentation per-region overlap (AUPRO) with 30% FPR [5] to explore the impact of anomaly detection performance on the multi-class classification. All metrics are calculated by the official code.

4.2. Quantitative results

We report the results of the multi-class anomaly classification on the MVTec AD and MTD datasets in Table 1 and 2. Notably, AnomalyNCD is compatible with all the anomaly detection methods to enable subsequent multi-class anomaly classification.

All methods in Table 1 only use unlabeled images as input. Compared to Anomaly Clustering [40], AnomalyNCD combined with zero-shot anomaly detection method MuSc [30], achieves 8.8% gains on NMI, 9.5% gains on ARI, and 10.8% F_1 gains, proving that AnomalyNCD extracts more discriminative features than Anomaly Clustering through contrastive learning in anomalous regions. AnomalyNCD also outperforms state-of-the-art NCD methods, achieving 16.1% gains on NMI, 18.0% gains on ARI, and 14.3% F_1 gains. The performance advantage of AnomalyNCD is due to focusing on anomalies inside images.

In Table 2, all methods utilize both unlabeled images and labeled normal images from the same product. We integrate AnomalyNCD with various one-class AD methods. Utilizing CPR, which has the highest AUPRO, achieves the best performance on the MVTec AD dataset: NMI increases by 10.7%, ARI by 14.9%, and F_1 score by 9.6%, surpassing other methods. On the MTD dataset, although the segmentation AUPRO of all AD methods is lower than that of Uniformly, PatchCore+AnomalyNCD still achieves improvements of 6.8% in ARI and 0.8% in F_1 score.

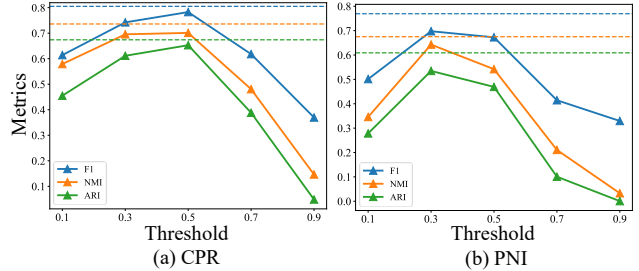


Figure 6. The results of various anomaly detection (AD) methods under multiple fixed thresholds. The horizontal dashed line represents the results of MEBin. Notably, the optimal fixed thresholds differ across AD methods, while our MEBin consistently outperforms the fixed threshold results.

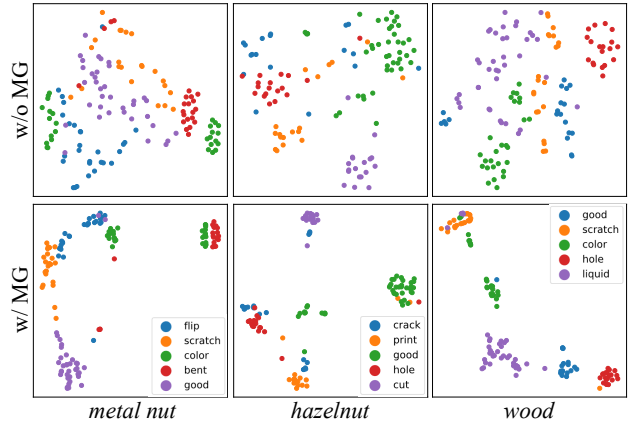


Figure 7. T-SNE visualization of sub-images on the MVTec AD dataset. We choose *metal nut*, *hazelnut* and *wood* as examples. The different colors of dots represent their anomaly classes.

4.3. Ablation Study

4.3.1. Effectiveness of main element binarization

Table 3 compares MEBin’s performance with the Otsu method [35] and fixed thresholds. Since the missed detection is more critical than over-detection in industrial scenarios, we define an anomaly as detected if the intersection over union (IoU) between the actual and predicted bounding boxes exceeds 0.1. Then we calculate the FPR and FNR for these binarization methods. MEBin demonstrates lower FPR and FNR than fixed thresholds and Otsu, leading to better multi-class classification results. Compared to the fixed thresholds, MEBin adaptively determines an optimal threshold for each image adaptation and achieves a 7.2% F_1 improvement. The Otsu tends to over-detect, particularly in normal images, making it less effective for this task.

In Fig. 6, we further apply MEBin on different one-class AD methods, which exhibit varying optimal fixed thresholds. For example, the optimal threshold of CPR [29] is near 0.5, whereas for PNI [2] it is approximately 0.3. MEBin’s adaptive threshold selection for each image outperforms all fixed thresholds for the whole image set.

| Mask Mechanism | NMI | ARI | F_1 |
|------------------------|--------------|--------------|--------------|
| (a) w/o MGA | 0.598 | 0.494 | 0.698 |
| (b) all tokens | 0.507 | 0.382 | 0.600 |
| (c) patch tokens | 0.563 | 0.467 | 0.686 |
| (d) class token (Ours) | 0.613 | 0.526 | 0.712 |

Table 4. Compared with different mask attention mechanisms on the MVTec AD dataset, the best-performing result is in bold.

| L_m | MVTec AD | | | MTD | | |
|-------|--------------|--------------|--------------|--------------|--------------|--------------|
| | NMI | ARI | F_1 | NMI | ARI | F_1 |
| 1 | 0.606 | 0.508 | 0.690 | 0.191 | 0.157 | 0.420 |
| 3 | 0.608 | 0.511 | 0.694 | 0.209 | 0.173 | 0.436 |
| 6 | 0.613 | 0.519 | 0.713 | 0.253 | 0.214 | 0.492 |
| 9 | 0.613 | 0.526 | 0.712 | 0.268 | 0.228 | 0.509 |
| 12 | 0.609 | 0.521 | 0.712 | 0.249 | 0.213 | 0.492 |

Table 5. Ablation study on the position of mask-guided layers on MVTec AD and MTD datasets. Best results in bold.

4.3.2. Discussion of the mask-guided attention

The mask-guided attention (MGA) directs ViT to focus on tokens within the mask (anomalous region). We show the t-SNE visualization in Fig. 7. With MGA in the 2nd row, image features have larger inter-class distances (e.g. *metal nut*) and smaller intra-class distances (e.g. *hazelnut* and *wood*) than those without MGA in the 1st row. In terms of metrics on MVTec AD, our MGA has a 1.5% NMI gain, 3.2% ARI gain, and 1.4% F_1 gain shown in Table 4.

We conduct experiments to introduce the binary mask into different tokens in Table 4. (b) introduces the binary mask on [CLS] token and patch tokens. (c) introduces it on patch tokens. Our MGA (d) only performs on [CLS] token, which is directly input into the classifier. We make patch tokens have a global receptive field to introduce more surrounding information indirectly into [CLS] token. Compared to other mask strategies, our MGA achieves 5.0% NMI, 5.9% ARI, and 2.6% F_1 improvements.

4.3.3. The influence of the mask-guided layer L_m

In our method, we introduce mask-guided attention in the last L_m layers of ViT. As reported in Table 5, we conduct the experiments with different L_m . The results demonstrate that using mask-guided attention in the last 9 layers yields better performance on both datasets. When L_m is small, the [CLS] token cannot adequately focus on the anomaly within the binary mask. In contrast, when $L_m = 12$, the [CLS] token completely lost contextual information around the anomaly, resulting in a drop in metrics.

4.3.4. Discussion of merging strategies

In Table 6, we report results using different merging strategies. (i) averaging the predictions of the sub-images, (ii) utilizing the anomaly scores of the sub-images as weights to merge, and (iii) using our region merging strategy. Strategy (iii) achieves better metrics than (i) and (ii) on both

| Merge | MVTec AD | | | MTD | | |
|----------------|--------------|--------------|--------------|--------------|--------------|--------------|
| | NMI | ARI | F_1 | NMI | ARI | F_1 |
| (i) Avg | 0.610 | 0.521 | 0.709 | 0.257 | 0.223 | 0.501 |
| (ii) Score Avg | 0.600 | 0.513 | 0.703 | 0.228 | 0.208 | 0.485 |
| (iii) Area Avg | 0.613 | 0.526 | 0.712 | 0.268 | 0.228 | 0.509 |

Table 6. Compared with different merging strategies on the MVTec AD and MTD datasets.

| | Precision | Recall | NMI | ARI | F_1 |
|---------|--------------|--------------|--------------|--------------|--------------|
| w/o PLC | 0.797 | 0.727 | 0.597 | 0.517 | 0.714 |
| w PLC | 0.821 | 0.876 | 0.613 | 0.526 | 0.712 |

Table 7. The ablation experiment of pseudo label correction (PLC) on the MVTec AD dataset. We evaluate the precision and recall of the normal class.

datasets. In anomaly detection, noise inevitably leads to over-detections, which have small areas but large anomaly scores. Directly averaging results over all sub-images is inaccurate, especially when many false positive sub-images are involved. Similarly, using anomaly scores as weights is also inappropriate. In contrast, our merging method, which assigns weights to multiple sub-image predictions based on area, achieves more robust merged predictions.

4.3.5. Effect of Pseudo Label Correcting

Our Pseudo Label Correcting (PLC) aims to reduce the impact of over-detections from the anomaly detection process. Although over-detected sub-images are normal, they have large appearance differences, which makes it difficult to correctly group them into the same normal class. Table 7 presents the precision and recall of the normal class. After applying PLC, recall improves by 14.9%, which means that some misclassified normal sub-images are corrected by our PLC. Additionally, a 1.6% improvement in NMI is observed in the multi-class classification results.

5. Conclusion

In this paper, we propose a novel multi-class anomaly classification method AnomalyNCD, which is compatible with existing anomaly detection methods. Firstly, we propose the main element binarization approach to isolate most over-detections and missed detections brought by anomaly detection methods. Secondly, we crop each anomalous region and leverage mask-guided representation learning to focus the network on the local anomaly and learn discriminative representations. Finally, our region merging strategy achieves flexible classification at sub-image and image levels during inference. While the performance of AnomalyNCD is generally influenced by the quality of the anomaly detection method, our AnomalyNCD outperforms all the current industrial anomaly clustering methods and NCD methods in the nature scene.

6. Acknowledgments

This work was supported by the National Natural Science Foundation of China under Grant No.62176098. The computation is completed in the HPC Platform of Huazhong University of Science and Technology.

References

- [1] Andrei-Timotei Ardelean and Tim Weyrich. Blind localization and clustering of anomalies in textures. *IEEE/CVF Conference on Computer Vision and Pattern Recognition Workshop (CVPR Workshop)*, 2024. 1
- [2] Jaehyeok Bae, Jae-Han Lee, and Seyun Kim. Pni: industrial anomaly detection using position and neighborhood information. In *IEEE/CVF International Conference on Computer Vision (ICCV)*, 2023. 6, 7
- [3] Anwesha Banerjee, Liyana Sahir Kallooriyakath, and Soma Biswas. Amend: Adaptive margin and expanded neighborhood for efficient generalized category discovery. In *IEEE/CVF Winter Conference on Applications of Computer Vision (WACV)*, 2024. 6, 7
- [4] Kilian Batzner, Lars Heckler, and Rebecca König. Efficientad: Accurate visual anomaly detection at millisecond-level latencies. In *IEEE/CVF Winter Conference on Applications of Computer Vision (WACV)*, 2024. 6
- [5] Paul Bergmann, Michael Fauser, David Sattlegger, and Carsten Steger. Mvtec ad—a comprehensive real-world dataset for unsupervised anomaly detection. In *IEEE/CVF Conference on Computer Vision and Pattern Recognition (CVPR)*, 2019. 2, 6, 7
- [6] Gedas Bertasius, Jianbo Shi, and Lorenzo Torresani. Deepedge: A multi-scale bifurcated deep network for top-down contour detection. In *IEEE/CVF Conference on Computer Vision and Pattern Recognition (CVPR)*, 2015. 2
- [7] Showmik Bhowmik, Ram Sarkar, Bishwadeep Das, and David Doermann. GiB: A Game Theory Inspired Binarization Technique for Degraded Document Images. *IEEE Transactions on Image Processing (TIP)*, 28(3):1443–1455, 2019. 2
- [8] Mathilde Caron, Ishan Misra, Julien Mairal, Priya Goyal, Piotr Bojanowski, and Armand Joulin. Unsupervised learning of visual features by contrasting cluster assignments. *Advances in Neural Information Processing Systems (NeurIPS)*, 2020. 5
- [9] Mathilde Caron, Hugo Touvron, Ishan Misra, Hervé Jégou, Julien Mairal, Piotr Bojanowski, and Armand Joulin. Emerging properties in self-supervised vision transformers. In *IEEE/CVF International Conference on Computer Vision (ICCV)*, 2021. 4, 5, 6
- [10] Yicong Chang, Feng Xue, Fei Sheng, Wenteng Liang, and Anlong Ming. Fast road segmentation via uncertainty-aware symmetric network. In *IEEE International Conference on Robotics and Automation (ICRA)*, 2022. 2
- [11] Ting Chen, Simon Kornblith, Mohammad Norouzi, and Geoffrey Hinton. A simple framework for contrastive learning of visual representations. In *International Conference on Machine Learning (ICML)*, 2020. 5
- [12] Bowen Cheng, Ishan Misra, Alexander G Schwing, Alexander Kirillov, and Rohit Girdhar. Masked-attention mask transformer for universal image segmentation. In *IEEE/CVF Conference on Computer Vision and Pattern Recognition (CVPR)*, 2022. 5
- [13] Alexey Dosovitskiy, Lucas Beyer, Alexander Kolesnikov, Dirk Weissenborn, Xiaohua Zhai, Thomas Unterthiner, Mostafa Dehghani, Matthias Minderer, Georg Heigold, Sylvain Gelly, et al. An image is worth 16x16 words: Transformers for image recognition at scale. In *International Conference on Learning Representations (ICLR)*, 2021. 4, 6
- [14] Jianan Fan, Dongnan Liu, Hang Chang, Heng Huang, Mei Chen, and Weidong Cai. Seeing unseen: Discover novel biomedical concepts via geometry-constrained probabilistic modeling. *IEEE/CVF Conference on Computer Vision and Pattern Recognition (CVPR)*, 2024. 2
- [15] Enrico Fini, Enver Sangineto, Stéphane Lathuilière, Zhun Zhong, Moin Nabi, and Elisa Ricci. A unified objective for novel class discovery. In *IEEE/CVF International Conference on Computer Vision (ICCV)*, 2021. 3, 6, 7
- [16] Shi Gong, Huan Zhou, Feng Xue, Cong Fang, Yiqun Li, and Yu Zhou. Fastroadseg: Fast monocular road segmentation network. *IEEE Transactions on Intelligent Transportation Systems (TITS)*, 23(11):21505–21514, 2022. 2
- [17] Peiyan Gu, Chuyu Zhang, Ruijie Xu, and Xuming He. Class-relation knowledge distillation for novel class discovery. In *IEEE/CVF International Conference on Computer Vision (ICCV)*, 2023. 3
- [18] Kai Han, Andrea Vedaldi, and Andrew Zisserman. Learning to discover novel visual categories via deep transfer clustering. In *IEEE/CVF International Conference on Computer Vision (ICCV)*, 2019. 2
- [19] Kai Han, Sylvestre-Alvise Rebuffi, Sebastien Ehrhardt, Andrea Vedaldi, and Andrew Zisserman. Autonovel: Automatically discovering and learning novel visual categories. *IEEE Transactions on Pattern Analysis and Machine Intelligence (TPAMI)*, 44(10):6767–6781, 2021. 2
- [20] Yen-Chang Hsu, Zhaoyang Lv, and Zsolt Kira. Learning to cluster in order to transfer across domains and tasks. In *International Conference on Learning Representations (ICLR)*, 2018. 2
- [21] Yen-Chang Hsu, Zhaoyang Lv, Joel Schlosser, Phillip Odom, and Zsolt Kira. Multi-class classification without multi-class labels. In *International Conference on Learning Representations (ICLR)*, 2019. 2
- [22] Bozhen Hu, Bin Gao, Wai Lok Woo, Lingfeng Ruan, Jikun Jin, Yang Yang, and Yongjie Yu. A lightweight spatial and temporal multi-feature fusion network for defect detection. *IEEE Transactions on Image Processing (TIP)*, 30:472–486, 2021. 1
- [23] Yibin Huang, Congying Qiu, and Kui Yuan. Surface defect saliency of magnetic tile. *The Visual Computer*, 36(1):85–96, 2020. 2, 6
- [24] Jongheon Jeong, Yang Zou, Taewan Kim, Dongqing Zhang, Avinash Ravichandran, and Onkar Dabeer. Winclip: Zero/few-shot anomaly classification and segmentation. In *IEEE/CVF Conference on Computer Vision and Pattern Recognition (CVPR)*, 2023. 1

- [25] Xu Ji, Joao F Henriques, and Andrea Vedaldi. Invariant information clustering for unsupervised image classification and segmentation. In *IEEE/CVF International Conference on Computer Vision (ICCV)*, 2019. 6
- [26] Prannay Khosla, Piotr Teterwak, Chen Wang, Aaron Sarna, Yonglong Tian, Phillip Isola, Aaron Maschiot, Ce Liu, and Dilip Krishnan. Supervised contrastive learning. *Advances in Neural Information Processing Systems (NeurIPS)*, 2020. 5
- [27] Harold W Kuhn. The hungarian method for the assignment problem. *Naval Research Logistics Quarterly*, 2(1-2):83–97, 1955. 7
- [28] Yujin Lee, Harin Lim, Seoyoon Jang, and Hyunsoo Yoon. Uniformly: Towards task-agnostic unified framework for visual anomaly detection. *arXiv preprint arXiv:2307.12540*, 2023. 1, 2, 6
- [29] Hanxi Li, Jianfei Hu, Bo Li, Hao Chen, Yongbin Zheng, and Chunhua Shen. Target before shooting: Accurate anomaly detection and localization under one millisecond via cascade patch retrieval. *IEEE Transactions on Image Processing (TIP)*, 33:5606–5621, 2024. 6, 7
- [30] Xurui Li, Ziming Huang, Feng Xue, and Yu Zhou. Musc: Zero-shot industrial anomaly classification and segmentation with mutual scoring of the unlabeled images. In *International Conference on Learning Representations (ICLR)*, 2024. 6, 7
- [31] Yufei Liang, Jiangning Zhang, Shiwei Zhao, Runze Wu, Yong Liu, and Shuwen Pan. Omni-frequency channel-selection representations for unsupervised anomaly detection. *IEEE Transactions on Image Processing (TIP)*, 32:4327–4340, 2023. 1
- [32] Christopher D Manning. *An introduction to Information Retrieval (IR)*. 2009. 7
- [33] Chuang Niu, Jun Zhang, Ge Wang, and Jimin Liang. Gat-cluster: Self-supervised gaussian-attention network for image clustering. In *European Conference on Computer Vision (ECCV)*, 2020. 6
- [34] Konstantinos Ntirogiannis, Basilis Gatos, and Ioannis Pratikakis. Performance evaluation methodology for historical document image binarization. *IEEE Transactions on Image Processing (TIP)*, 22(2):595–609, 2013. 2
- [35] Nobuyuki Otsu. A threshold selection method from gray-level histograms. *IEEE Transactions on Systems, Man, and Cybernetics (TSMC)*, 9(1):62–66, 1979. 2, 7
- [36] William M Rand. Objective criteria for the evaluation of clustering methods. *Journal of the American Statistical Association (JASA)*, 66(336):846–850, 1971. 7
- [37] Luigi Riz, Cristiano Saltori, Elisa Ricci, and Fabio Poiesi. Novel class discovery for 3d point cloud semantic segmentation. In *IEEE/CVF Conference on Computer Vision and Pattern Recognition (CVPR)*, 2023. 2
- [38] Karsten Roth, Latha Pemula, Joaquin Zepeda, Bernhard Schölkopf, Thomas Brox, and Peter Gehler. Towards total recall in industrial anomaly detection. In *IEEE/CVF Conference on Computer Vision and Pattern Recognition (CVPR)*, 2022. 6
- [39] Sudipta Roy, Ayan Dey, Kingshuk Chatterjee, and Samir K Bandyopadhyay. A new efficient binarization method for mri of brain image. *Signal & Image Processing*, 3(6):35, 2012. 2
- [40] Kihyuk Sohn, Jinsung Yoon, Chun-Liang Li, Chen-Yu Lee, and Tomas Pfister. Anomaly clustering: Grouping images into coherent clusters of anomaly types. In *IEEE/CVF Winter Conference on Applications of Computer Vision (WACV)*, 2023. 1, 2, 6, 7
- [41] Bolan Su, Shijian Lu, and Chew Lim Tan. Robust document image binarization technique for degraded document images. *IEEE Transactions on Image Processing (TIP)*, 22(4):1408–1417, 2012. 2
- [42] Torbjørn Sund and Karsten Eilertsen. An algorithm for fast adaptive image binarization with applications in radiotherapy imaging. *IEEE Transactions on Medical Imaging (TMI)*, 22(1):22–28, 2003. 2
- [43] Tran Dinh Tien, Anh Tuan Nguyen, Nguyen Hoang Tran, Ta Duc Huy, Soan Duong, Chanh D Tr Nguyen, and Steven QH Truong. Revisiting reverse distillation for anomaly detection. In *IEEE/CVF Conference on Computer Vision and Pattern Recognition (CVPR)*, 2023. 6
- [44] Wouter Van Gansbeke, Simon Vandenhende, Stamatios Georgoulis, Marc Proesmans, and Luc Van Gool. Scan: Learning to classify images without labels. In *European Conference on Computer Vision (ECCV)*, 2020. 6
- [45] Sagar Vaze, Kai Han, Andrea Vedaldi, and Andrew Zisserman. Generalized category discovery. In *IEEE/CVF Conference on Computer Vision and Pattern Recognition (CVPR)*, 2022. 3, 5, 6, 7
- [46] Sagar Vaze, Andrea Vedaldi, and Andrew Zisserman. No representation rules them all in category discovery. *Advances in Neural Information Processing Systems (NeurIPS)*, 2023. 2
- [47] Xin Wen, Bingchen Zhao, and Xiaojuan Qi. Parametric classification for generalized category discovery: A baseline study. In *IEEE/CVF International Conference on Computer Vision (ICCV)*, 2023. 5, 6, 7
- [48] Weijia Wu, Yuzhong Zhao, Mike Zheng Shou, Hong Zhou, and Chunhua Shen. Diffumask: Synthesizing images with pixel-level annotations for semantic segmentation using diffusion models. In *IEEE/CVF International Conference on Computer Vision (ICCV)*, 2023. 2
- [49] Ruijie Xu, Chuyu Zhang, Hui Ren, and Xuming He. Dual-level adaptive self-labeling for novel class discovery in point cloud segmentation. In *European Conference on Computer Vision (ECCV)*. Springer, 2025. 2
- [50] Feng Xue, Anlong Ming, and Yu Zhou. A novel multi-layer framework for tiny obstacle discovery. In *International Conference on Robotics and Automation (ICRA)*, 2019. 2
- [51] Feng Xue, Anlong Ming, and Yu Zhou. Tiny obstacle discovery by occlusion-aware multilayer regression. *IEEE Transactions on Image Processing (TIP)*, 29:9373–9386, 2020.
- [52] Feng Xue, Yicong Chang, Tianxi Wang, Yu Zhou, and Anlong Ming. Indoor obstacle discovery on reflective ground via monocular camera. *International Journal of Computer Vision (IJCV)*, 132(3):987–1007, 2024. 2
- [53] Zhaoyang Zeng, Bei Liu, Jianlong Fu, and Hongyang Chao. Reference-based defect detection network. *IEEE Transactions on Image Processing (TIP)*, 30:6637–6647, 2021. 1

- [54] Zilong Zhang, Zhibin Zhao, Xingwu Zhang, Chuang Sun, and Xuefeng Chen. Industrial anomaly detection with domain shift: A real-world dataset and masked multi-scale reconstruction. *Computers in Industry*, 151:103990, 2023. [6](#)
- [55] Yuyang Zhao, Zhun Zhong, Nicu Sebe, and Gim Hee Lee. Novel class discovery in semantic segmentation. In *IEEE/CVF Conference on Computer Vision and Pattern Recognition (CVPR)*, 2022. [2](#)
- [56] Zhun Zhong, Linchao Zhu, Zhiming Luo, Shaozi Li, Yi Yang, and Nicu Sebe. Openmix: Reviving known knowledge for discovering novel visual categories in an open world. In *IEEE/CVF Conference on Computer Vision and Pattern Recognition (CVPR)*, 2021. [2](#)
- [57] Huan Zhou, Feng Xue, Yucong Li, Shi Gong, Yiqun Li, and Yu Zhou. Exploiting low-level representations for ultra-fast road segmentation. *IEEE Transactions on Intelligent Transportation Systems (TITS)*, pages 1–11, 2024. [2](#)
- [58] Jiaying Zhou, Yang Liu, and Qingchao Chen. Novel class discovery in chest x-rays via paired images and text. In *Proceedings of the AAAI Conference on Artificial Intelligence (AAAI)*, 2024. [2](#)
- [59] Yu Zhou, Rui Lu, Feng Xue, and Yuzhe Gao. Occlusion relationship reasoning with a feature separation and interaction network. *Visual Intelligence*, 1(1):23, 2023. [2](#)

AnomalyNCD: Towards Novel Anomaly Class Discovery in Industrial Scenarios

Supplementary Material

Overview

In this appendix, we provide additional descriptions of the following contents:

- Training details for novel class discovery (Sec. A).
- The implementation details about our experiment settings (Sec. B).
- The implementation details of our cropping method (Sec. C).
- Discussion of the anomaly-centered sub-image cropping (Sec. D).
- Discussion of the vision transformer under a supervised setting (Sec. E).
- Discussion of the labeled abnormal images (Sec. F).
- Discussion on handling the combined category (Sec. G).
- The computational analysis (Sec. H).
- The analysis of model performance using ground truth masks (Sec. I).
- Ablation study on the number of threshold index in MEBin (Sec. J).
- The sensitivity analysis of the hyperparameter τ in MEBin (Sec. K).
- Sensitivity analysis of threshold 0.5 in PLC (Sec. L).
- The binarization results of MEBin (Sec. M).
- More detailed t-SNE visualizations (Sec. N).
- More detailed quantitative results (Sec. O).
- Limitation (Sec. P).

A. Training details for novel class discovery

We present concrete implementations of the novel class discovery paradigm used in our method. Following [? ?], we employ both classification learning and contrastive representation learning to train the network. For each sub-image $x_{i,k}$, we use a new subscript j to replace i, k for a simple and clear description. Thus the augmented views of x_j are formed as (\tilde{x}_j, \hat{x}_j) . These views are fed into MGViT, denoted as $f(\cdot)$, to extract the [CLS] tokens.

- For labeled sub-images, the ground truth labels are available. Therefore, we employ both self-supervised contrastive learning and supervised contrastive learning. In addition, supervised classification learning is performed by treating the ground truth labels as optimization targets.
- For unlabeled sub-images, we use self-supervised contrastive representation learning. The pseudo labels are generated to perform classification learning.

Contrastive representation learning. The [CLS] tokens extracted by MGViT are fed into a three-layer MLP, denoted as $\phi(\cdot)$, to generate the image features from \tilde{x}_j and \hat{x}_j : $\tilde{z}_j = \phi(f(\tilde{x}_j))$ and $\hat{z}_j = \phi(f(\hat{x}_j))$. For both labeled

and unlabeled sub-images, we employ the self-supervised contrastive loss \mathcal{L}_{rep} as,

$$\mathcal{L}_{\text{rep}} = \frac{1}{|B|} \sum_{j \in B} -\log \frac{\exp(\hat{z}_j^\top \tilde{z}_j / \tau_u)}{\sum_{n \in \mathcal{N}_j} \exp(\hat{z}_j^\top \tilde{z}_n / \tau_u)} \quad (7)$$

where B denotes a mini-batch. $|B|$ represents the number of image pairs in B . \mathcal{N}_j indexes other image pairs in the batch except (\hat{x}_j, \tilde{x}_j) , and τ_u is a temperature value. Similarly, the supervised contrastive loss for labeled data is written as:

$$\mathcal{L}_{\text{rep}}^1 = \frac{1}{|B^1|} \sum_{j \in B^1} \frac{1}{|\mathcal{P}_j|} \sum_{p \in \mathcal{P}_j} -\log \frac{\exp(\hat{z}_j^\top \tilde{z}_p / \tau_c)}{\sum_{n \in \mathcal{N}_j} \exp(\hat{z}_j^\top \tilde{z}_n / \tau_c)} \quad (8)$$

where $B^1 \subset B$ represents the indexes of labeled images in the batch B . \mathcal{P}_j indexes other images in the batch B which have the same labels as \hat{x}_j and \tilde{x}_j . τ_c is a temperature value.

Classification learning. For each image pair (\hat{x}_j, \tilde{x}_j) in a batch, we feed them into the teacher and student networks respectively, which have shared MGViT and classification heads with different softmax temperatures. For labeled sub-images, we convert the ground truth label into the one-hot vector $\hat{y}_j = \tilde{y}_j \in \mathbb{R}^{1 \times (\mathcal{C}^1 + \mathcal{C}^u)}$, where the entry corresponding to the target class is set to 1 and all other entries are 0. For unlabeled sub-images \tilde{x}_j, \hat{x}_j , we generate pseudo labels \hat{q}_j, \tilde{q}_j by the “teacher” one, which employs a sharp temperature τ_t to produce confident predictions. Specifically, following DINO [65], we compute the logits for two views (\hat{x}_j, \tilde{x}_j) as $\hat{l}_j = \mathcal{H}(f(\hat{x}_j))$ and $\tilde{l}_j = \mathcal{H}(f(\tilde{x}_j))$, where $\hat{l}_j, \tilde{l}_j \in \mathbb{R}^{1 \times (\mathcal{C}^1 + \mathcal{C}^u)}$, $f(\cdot)$ indicates MGViT that outputs the [CLS] token, and $\mathcal{H}(\cdot)$ is the linear classifier. Then, a softmax with temperature τ_t converts these logits into pseudo labels $\hat{q}_j, \tilde{q}_j \in \mathbb{R}^{1 \times (\mathcal{C}^1 + \mathcal{C}^u)}$ as follows,

$$\hat{q}_j^{(k)} = \frac{\exp(\hat{l}_j^{(k)} / \tau_t)}{\sum_{k=1}^{\mathcal{C}^1 + \mathcal{C}^u} \exp(\hat{l}_j^{(k)} / \tau_t)} \quad (9)$$

where $\hat{q}_j^{(k)}$ and $\hat{l}_j^{(k)}$ denote the pseudo-label value and logit value respectively for the k -th class in $\mathcal{C}^1 + \mathcal{C}^u$. Note that, we set the logits \tilde{l}_j, \hat{l}_j for \mathcal{C}^1 known classes to $-\infty$ to isolate known classes when calculating pseudo labels. Then the pseudo-label values for the known classes calculated by Eq. (9) are 0. The “student” one, using a smooth temperature τ_s , generates the probability predictions $\hat{p}_j \in \mathbb{R}^{1 \times (\mathcal{C}^1 + \mathcal{C}^u)}$ for sub-image \hat{x}_j as,

$$\hat{p}_j^{(k)} = \frac{\exp(\hat{l}_j^{(k)} / \tau_s)}{\sum_{k=1}^{\mathcal{C}^1 + \mathcal{C}^u} \exp(\hat{l}_j^{(k)} / \tau_s)} \quad (10)$$

where $\hat{p}_j^{(k)}$ denotes the prediction probability for the k -th class in $\mathcal{C}^l + \mathcal{C}^u$. The student network is trained to align \hat{p}_j , \tilde{p}_j with either the ground truth labels (for labeled data) or the pseudo labels (for unlabeled data). With the representation above, we leverage the standard cross-entropy loss $\mathcal{L}_{\text{CE}}(p, q) = -\sum_{c=0}^{\mathcal{C}^l + \mathcal{C}^u - 1} p^c \log q^c$ to optimize the classification, which is represented as:

$$\mathcal{L}_{\text{cls}}^l = \frac{1}{|B^l|} \sum_{j \in B^l} (\mathcal{L}_{\text{CE}}(\hat{y}_j, \tilde{p}_j) + \mathcal{L}_{\text{CE}}(\tilde{y}_j, \hat{p}_j)) \quad (11)$$

$$\mathcal{L}_{\text{cls}}^u = \frac{1}{|B^u|} \sum_{j \in B^u} (\mathcal{L}_{\text{CE}}(\hat{q}_j, \tilde{p}_j) + \mathcal{L}_{\text{CE}}(\tilde{q}_j, \hat{p}_j)) \quad (12)$$

where B^u indexes the unlabeled images of the batch B .

Finally, we adopt a mean-entropy maximization regularizer [64] $\mathcal{L}_{\text{reg}}^u = \mathcal{L}_{\text{CE}}(\bar{p}_j, \tilde{p}_j)$ for unlabeled sub-images, where $\bar{p}_j = \frac{1}{2|B^u|} \sum_{j \in B^u} (\hat{p}_j + \tilde{p}_j)$ denotes the mean prediction of unlabeled images. The overall loss of training objective is written as:

$$\mathcal{L} = \lambda(\mathcal{L}_{\text{rep}}^l + \mathcal{L}_{\text{cls}}^l) + (1 - \lambda)(\mathcal{L}_{\text{rep}} + \mathcal{L}_{\text{cls}}^u + \mu\mathcal{L}_{\text{reg}}^u) \quad (13)$$

where λ is a hyperparameter that balances the supervised loss and the self-supervised loss. μ is the coefficient of the regularization.

B. Additional implementation details

We use ViT-B/8 [67] pre-trained with DINO [65] as our feature extractor. The self-attentions in the last 9 layers are replaced with our mask-guided attention. During training, all the layers of ViT are fixed except the last layer. As with UNO[68] and BYOP[78], we use the multi-head strategy in the classifier \mathcal{H} , and use the head with the smallest loss for inference. The input images are scaled to a resolution of 224×224 . We set the batch size to 32 and epochs to 50. The Stochastic Gradient Descent (SGD) optimizer [63] is employed with a learning rate of 0.003. To generate two augmented views for contrastive learning, we follow the data augmentation strategies in BYOL [69] (random crop, flip, color jittering, and Gaussian blur) and RandAug [66] (rotation, posterize, and sharpness). Aligning with [?], the temperature values are set as follows: τ_u is 0.07 and τ_c is 1.0, τ_s is set to 0.1 and τ_t is initialized to 0.07. For the first 40 epochs, τ_t reduces every 4 epochs, linearly down to 0.04, then stays the same. For our Main Element Binarization approach, we set the \mathcal{T} to 64 and τ to 4. In the overall loss, the parameters λ and μ are set to 0.3 and 4 respectively. In the Region Merging strategy, the temperature τ_α is set to 100 on the MVTEC AD dataset and 50 on the MTD dataset.

For anomaly detection methods preceding AnomalyNCD, we choose zero-shot method MuSc [73], one-class methods PatchCore [75], EfficientAD [61], RD++ [77], PNI [60] and CPR [72]. Note that CPR does not provide the

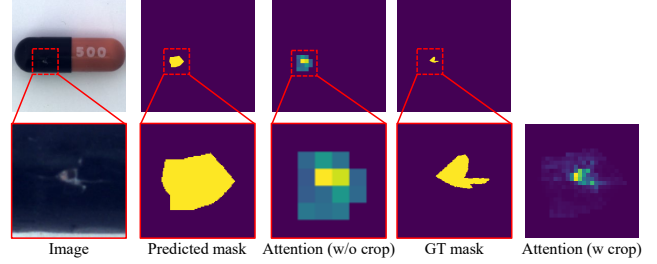


Figure 8. **Visualization of [CLS] tokens’s attention** for entire image and sub-image.

training code, we directly use the official checkpoints on the MVTEC AD dataset. EfficientAD does not release official implementation, we use the unofficial version. For RD++ and PNI, we conduct experiments on the MTD dataset according to the configuration of MVTEC AD.

C. Implementation details of cropping

For each region in M_i^u , we set a square box that completely encloses this region but has minimal area. Then we extend each square box by adding a 10% padding. The padding area includes the background of anomalies and thus enables our network to extract features indicating the anomaly’s position on products, which is critical for classification. Notice that we keep the minimum crop size as 1% of the image size. Finally, along each square box of M_i^u , we crop a sub-image from I_i^u and its mask from M_i^u .

D. Discussion of the anomaly-centered sub-image cropping

The cropping operation plays a crucial role in industrial anomaly clustering for two primary reasons. First, many anomalies in industrial products are local and subtle. The cropping operation makes the anomalous region occupy most of the image, which helps the network learn the anomaly easily. Second, the cropping operation can handle images with *combined* type anomalies, where there are different types of anomalies in an image. More details about *combined* type anomalies are given in Sec. G.

As shown in Fig. 8, for the original image, the attention of [CLS] token has a coarse-grained response in the anomalous region. When the anomaly is subtle, the discriminative features are hard to learn. For the sub-image, the attention has a fine-grained response and learns the more discriminative pixels of subtle anomaly. We report multi-class classification on the MVTEC AD and MTD datasets in Table 8. Since anomalies on the MTD dataset are subtle and finer, the crop operation is required for fine-grained feature learning, which can bring up to 23.8% NMI improvement for PatchCore+AnomalyNCD and 11.5% NMI

| Dataset | Setting | MuSc[73]+AnomalyNCD | | | PatchCore[75]+AnomalyNCD | | | EfficientAD[61]+AnomalyNCD | | | PNI[60]+AnomalyNCD | | |
|---------------|----------|---------------------|--------------|--------------|--------------------------|--------------|--------------|----------------------------|--------------|--------------|--------------------|--------------|--------------|
| | | NMI | ARI | F_1 | NMI | ARI | F_1 | NMI | ARI | F_1 | NMI | ARI | F_1 |
| MVTec AD [62] | w/o crop | 0.622 | 0.549 | 0.740 | 0.650 | 0.584 | 0.755 | 0.501 | 0.396 | 0.637 | 0.676 | 0.616 | 0.777 |
| | w crop | 0.613 | 0.526 | 0.712 | 0.670 | 0.601 | 0.769 | 0.516 | 0.394 | 0.641 | 0.675 | 0.609 | 0.769 |
| MTD [70] | w/o crop | 0.086 | 0.076 | 0.374 | 0.142 | 0.166 | 0.432 | 0.105 | 0.066 | 0.379 | 0.107 | 0.134 | 0.407 |
| | w crop | 0.268 | 0.228 | 0.509 | 0.380 | 0.390 | 0.617 | 0.220 | 0.188 | 0.467 | 0.181 | 0.219 | 0.465 |

Table 8. Ablation of Anomaly-Centered Sub-Image Cropping on the MVTec AD and MTD datasets.

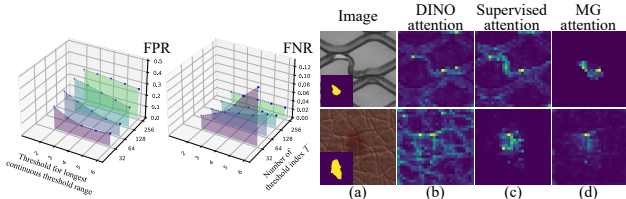


Figure 9. Ablation study on \mathcal{T} in MEBin. Figure 10. Visualization of self-attention of the [CLS] token.

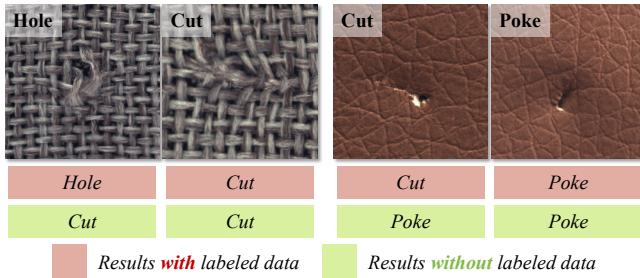


Figure 11. **Impact of using or not using labeled data.** We show two product cases, and each presents two similar anomalies.

gains for EfficientAD+AnomalyNCD. On the MVTec AD dataset, the crop operation results in a 2.0% NMI increase for PatchCore+AnomalyNCD and 1.5% NMI gain for EfficientAD+AnomalyNCD. When using MuSc or PNI as the anomaly detection method, it only decreases NMI by 0.9% at most.

E. Discussion of ViT under a supervised setting

To study the ability of the vision transformer (ViT) to focus on local anomalies under a supervised setting, we leave one out cross validation. As shown in the attention maps of Fig. 10, the supervised training could focus on the anomaly regions, while it needs manually collecting and labeling the abnormal samples, which is time-consuming. As shown in (c) and (d), our AnomalyNCD leverages self-supervision to reduce these manual operations while also focuses attention on the anomalies, which is more suitable for industrial scenarios.

| | MVTec AD | | | MTD | | |
|---------------------|--------------|--------------|--------------|--------------|--------------|--------------|
| | NMI | ARI | F_1 | NMI | ARI | F_1 |
| w/o \mathcal{D}^1 | 0.583 | 0.506 | 0.689 | 0.227 | 0.202 | 0.485 |
| w \mathcal{D}^1 | 0.613 | 0.526 | 0.712 | 0.268 | 0.228 | 0.509 |

Table 9. The ablation experiment of using labeled abnormal images \mathcal{D}^1 on the MVTec AD and MTD datasets.

F. Discussion of the labeled abnormal images

As shown in Fig. 11, labeled data is significant for our mask-guided representation learning (MGRL). If only using unlabeled data, MGRL is prone to confuse anomalies with highly similar appearances. For example, a ‘‘Hole’’ on a carpet is treated as ‘‘Cut’’, and ‘‘Cut’’ on leather is misclassified as a ‘‘Poke’’. Actually, even humans tend to confuse them. With the supervision of labeled data, confusion does not occur. The reason is that the labeled data helps to build the feature space of prior classes, so that even the subtle differences from novel classes can be recognized.

In the labeled abnormal images \mathcal{D}^1 , there is much prior knowledge of industrial anomalies classification, such as anomalies with similar size, color, and location belonging to the same class. Using them to train the network together can transfer the knowledge from \mathcal{D}^1 to the network and separate confusing anomalies from each other in \mathcal{D}^u . We report the quantitative results in Table 9, using \mathcal{D}^1 brings 3.0% NMI improvements on MVTec AD and 3.9% NMI improvements on MTD. In addition, we also use 15 categories in the MVTec AD dataset as the labeled abnormal images in turn. Except for the *toothbrush* category, which has only one anomaly class. The quantitative results are reported in Tables 10 to 12. MuSc is used as the anomaly detection method by default.

G. Discussion on handling the combined category

In main experiments, we follow Anomaly Clustering [76] to remove the combined class for a fair comparison. However, the combined class is quite common in the industrial scene, such as the *cable*, *pill*, *wood*, and *zipper* products on the MVTec AD dataset. The image with the combined class

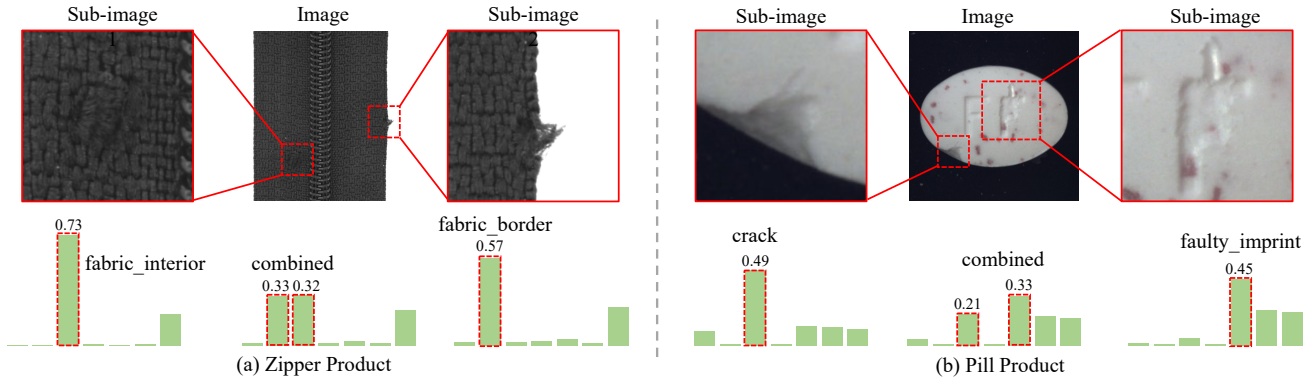


Figure 12. **Multi-class classification results of two combined-type anomaly images.** Taking “zipper” and “pill” as examples, we show the predicted probabilities for each sub-image individually and for the entire image.

| | (II) | (III) | (IV) | Total |
|-----------|-------|-------|------|-------|
| Time (ms) | 129.8 | 22.8 | 0.5 | 153.1 |

Table 13. Inference time for each module on a per-image basis.

contains multiple different types of anomalies, yet current clustering methods can only classify the entire image into one anomaly type. For our method, we crop the image into many sub-images, and the classifier assigns each sub-image a label. In this way, all the anomalous regions in the combined image can be found and classified individually. As shown in Fig. 12, there are two types of anomalies in the zipper and pill products respectively. Each anomalous region is cropped and correctly classified. By merging the prediction of the sub-images to the entire image, we find that classifying the image as these two types of anomalies has a higher probability.

H. Computational analysis

We measure the inference speed of AnomalyNCD on an NVIDIA RTX 3090 GPU. The entire inference process consists of four steps: (I) applying an anomaly detection method to the input image, (II) binarizing the anomaly map and cropping sub-images accordingly, (III) feeding these sub-images and their corresponding masks into our mask-guided ViT and getting probability output, and (IV) merging predictions from each sub-image to generate the final output. Table 13 presents the per-image inference time for each step. Note that the time taken for step (I) depends on the anomaly detection method and is independent of our AnomalyNCD. The majority of the inference time is concentrated in the MEBin and image cropping, which account for over 80% of the total runtime. MEBin uses the official OpenCV library for connection component calculations, resulting in the inability to use CUDA acceleration.

| Methods | MVTec AD | | | MTD | | |
|---------|--------------|--------------|--------------|--------------|--------------|--------------|
| | NMI | ARI | F_1 | NMI | ARI | F_1 |
| AC [76] | 0.711 | 0.638 | 0.718 | 0.467 | 0.359 | 0.482 |
| Ours | 0.871 | 0.851 | 0.909 | 0.829 | 0.863 | 0.841 |

Table 14. The quantitative results of using the ground truth masks. We compare our AnomalyNCD with Anomaly Clustering on the MVTec AD and MTD datasets.

I. Analysis of model performance using ground truth masks

In the experimental section, we demonstrate that our multi-class classification performs better when the anomaly detection method performs better. So in order to test the optimal results of our AnomalyNCD, we assume an ideal anomaly detection method where the ground truth masks of unlabeled images are available. We report the results in Table 14, our approach achieves significant improvement over Anomaly Clustering on two datasets. On MVTec AD, there is a 16.0% improvement on the NMI and a 19.1% improvement on the F_1 , and on MTD, there is a 36.2% improvement on the NMI and a 35.9% improvement on the F_1 . In this ideal case, ground truth masks do not introduce any over-detections and missed detections compared to anomaly maps generated by anomaly detection methods. With the improvement of anomaly detection methods in the future, our AnomalyNCD can achieve better results.

J. Ablation study on the number of threshold index in MEBin

In Fig. 9, we conduct the ablation study on the number of threshold index \mathcal{T} . Note that we use powers of 2 for candidates of \mathcal{T} , since it is calculated on grayscale images (0-255). $\mathcal{T} = 64$ achieves better FPR-FNR trade-off compared to other \mathcal{T} . With a small value ($\mathcal{T} = 32$), the binary mask

| PLC Thresholds | MVTec AD - MuSc | MTD - MuSc | MVTec AD - RD++ | MTD - RD++ | MVTec AD - PatchCore | MTD - PatchCore | Rank |
|----------------|--------------------------|--------------------------|--------------------------|--------------------------|--------------------------|--------------------------|-------------|
| 0.1 | 0.602/0.522/0.715 | 0.212/0.180/0.419 | 0.625/0.531/0.717 | 0.368/0.377/0.587 | 0.630/0.574/0.734 | 0.457/0.453/0.683 | 3.44 |
| 0.3 | 0.615/0.533/0.727 | 0.230/0.204/0.487 | 0.627/0.545/0.721 | 0.391/0.382/0.595 | 0.646/0.594/0.757 | 0.466/0.452/0.683 | 2.28 |
| 0.5 | 0.613/0.526/0.712 | 0.268/0.228/0.509 | 0.631/0.542/0.721 | 0.368/0.361/0.600 | 0.670/0.601/0.769 | 0.380/0.390/0.715 | 2.17 |
| 0.7 | 0.630/0.557/0.731 | 0.257/0.212/0.489 | 0.650/0.561/0.741 | 0.353/0.333/0.566 | 0.653/0.578/0.748 | 0.602/0.415/0.664 | 2.22 |
| 0.9 | 0.584/0.476/0.682 | 0.231/0.172/0.489 | 0.604/0.487/0.682 | 0.337/0.302/0.549 | 0.506/0.338/0.610 | 0.423/0.352/0.660 | 4.67 |

Table 15. The results (NMI, ARI, F1) on two datasets, when taking various PLC thresholds. **Rank** is the average ranking of the threshold.

| | MuSc[73]+AnomalyNCD | | | CPR[72]+AnomalyNCD | | |
|------------|---------------------|--------|--------|--------------------|--------|--------|
| | NMI | ARI | F_1 | NMI | ARI | F_1 |
| $\tau = 2$ | 0.640 | 0.537 | 0.707 | 0.720 | 0.647 | 0.787 |
| $\tau = 3$ | 0.647 | 0.543 | 0.718 | 0.736 | 0.668 | 0.797 |
| $\tau = 4$ | 0.613 | 0.526 | 0.712 | 0.736 | 0.674 | 0.805 |
| $\tau = 5$ | 0.618 | 0.539 | 0.740 | 0.721 | 0.665 | 0.807 |
| $\tau = 6$ | 0.600 | 0.510 | 0.715 | 0.710 | 0.655 | 0.799 |
| variance | 0.0003 | 0.0001 | 0.0001 | 0.0001 | 0.0001 | 0.0001 |

Table 16. Sensitivity analysis of the minimum stable range τ in MEBin. We use the zero-shot AD method MuSc and one-class AD method CPR to conduct experiments.

changes dramatically, making it difficult to determine a stable connected component. Conversely, a larger \mathcal{T} brings more time consumption. Therefore, we set $\mathcal{T} = 64$ as the default value.

K. Sensitivity analysis of τ in MEBin

In Table 16, we experiment with the parameter sensitivity of the minimum stable range τ on the MVTEC AD dataset. We use the zero-shot anomaly detection method MuSc [73] and the one-class method CPR [72] respectively to combine with our AnomalyNCD. When the hyperparameter τ is changed, the multi-class anomaly classification results change with a variance of about 0.0001, demonstrating that our method is insensitive to τ .

L. Sensitivity analysis of threshold 0.5 in PLC

Although MEBin achieves a decent trade-off, it may still get over-detections due to local noises. Thus, PLC uses the threshold 0.5 to find over-detections and corrects their pseudo label with a normal one-hot label. The optimal PLC threshold is related to datasets and anomaly detection methods. Tab. 15 shows the results of three methods on two datasets, when taking various PLC thresholds. Observably, a threshold of 0.5 ranks 1st performance on average in all candidates.

M. Binarization results of MEBin

From Fig. 16 to Fig. 18, we binarize the anomaly maps output by MuSc [73] using different binarization strategies, including the fixed threshold, the Otsu [74] method, and our MEBin. Our binarization strategy does not require the validation set to determine a threshold and adaptively obtain

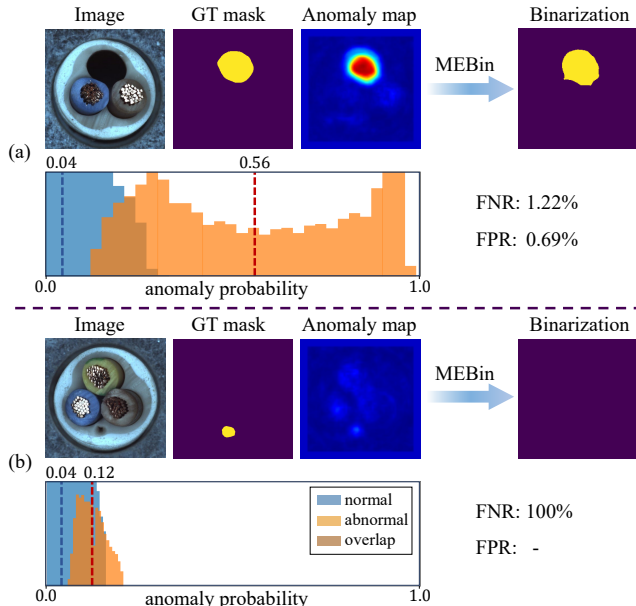


Figure 13. **Analysis of anomaly maps in EfficientAD.** We visualize the pixel-level anomaly probability histogram, and use dashed lines to represent the average anomaly probability for normal and anomalous regions respectively.

the optimal threshold for each image with fewer false positives and false negatives. Compared to the Otsu method, our MEBin has fewer false positives, especially on normal images. We also report the optimal threshold searched by our MEBin in the last column of Fig. 16 to Fig. 18. The optimal threshold ranges from 0.380 to 1.000, making it difficult to handle all situations with a fixed threshold.

N. Detailed t-SNE visualization

In Fig. 14, we show more t-SNE visualization on all the products of the MVTEC AD dataset. We also provide more qualitative comparisons with AC [76] and Uniformly [71] in Fig. 15. These methods show slight clustering phenomena, while our AnomalyNCD has larger inter-class distances and smaller intra-class distances. This further proves the superiority of our method from the qualitative perspective.

O. Detailed quantitative results

In this section, we report the detailed results of our AnomalyNCD combined with various anomaly detection methods on the MVTec AD dataset, as shown in Table 17.

P. Limitation

The anomaly detection methods used affect the performance of our AnomalyNCD. In general, if the anomaly detection method has a higher AUPRO, we can achieve a better performance in the multi-class anomaly classification task. In the ideal situation where the ground truth mask is available (AUPRO=100%), our AnomalyNCD is significantly superior to other methods, which has been discussed in Sec. I. However, EfficientAD [61] is an exception, with a lower multi-class anomaly classification performance despite higher AUPRO. We observe that a large span of anomaly probability values exists between different anomaly maps generated by EfficientAD, as shown in Fig. 13. The average value of the anomalous region in (a) is only 0.12, which is close to the anomaly probability in the normal region, while that in (b) is 0.56. This large span causes false negatives in (a) during binarization, resulting in a lower performance for anomaly classification.

| Methods | MuSc[73] | | | PatchCore[75] | | | EfficientAD[61] | | | RD++[77] | | | PNI[60] | | | CPR[72] | | |
|-----------------|-------------|-------|----------------|---------------|-------|----------------|-----------------|-------|----------------|-------------|-------|----------------|-------------|-------|----------------|-------------|-------|----------------|
| | +AnomalyNCD | | | +AnomalyNCD | | | +AnomalyNCD | | | +AnomalyNCD | | | +AnomalyNCD | | | +AnomalyNCD | | |
| Products\Metric | NMI | ARI | F ₁ | NMI | ARI | F ₁ | NMI | ARI | F ₁ | NMI | ARI | F ₁ | NMI | ARI | F ₁ | NMI | ARI | F ₁ |
| bottle | 0.613 | 0.583 | 0.819 | 0.734 | 0.671 | 0.855 | 0.544 | 0.467 | 0.759 | 0.640 | 0.529 | 0.771 | 0.676 | 0.598 | 0.819 | 0.775 | 0.757 | 0.904 |
| cable | 0.597 | 0.492 | 0.626 | 0.758 | 0.666 | 0.741 | 0.549 | 0.414 | 0.619 | 0.679 | 0.602 | 0.734 | 0.765 | 0.601 | 0.691 | 0.711 | 0.476 | 0.561 |
| capsule | 0.445 | 0.335 | 0.591 | 0.402 | 0.277 | 0.530 | 0.519 | 0.402 | 0.644 | 0.481 | 0.392 | 0.606 | 0.425 | 0.338 | 0.568 | 0.549 | 0.438 | 0.674 |
| carpet | 0.852 | 0.837 | 0.906 | 0.628 | 0.569 | 0.726 | 0.672 | 0.577 | 0.726 | 0.599 | 0.527 | 0.658 | 0.619 | 0.548 | 0.701 | 0.740 | 0.638 | 0.795 |
| grid | 0.622 | 0.578 | 0.731 | 0.670 | 0.581 | 0.731 | 0.684 | 0.570 | 0.795 | 0.631 | 0.544 | 0.615 | 0.583 | 0.534 | 0.705 | 0.766 | 0.689 | 0.731 |
| hazelnut | 0.662 | 0.582 | 0.718 | 0.859 | 0.875 | 0.927 | 0.570 | 0.429 | 0.673 | 0.845 | 0.853 | 0.909 | 0.919 | 0.926 | 0.955 | 0.723 | 0.727 | 0.827 |
| leather | 0.863 | 0.838 | 0.911 | 0.770 | 0.734 | 0.839 | 0.587 | 0.449 | 0.621 | 0.746 | 0.688 | 0.782 | 0.672 | 0.616 | 0.734 | 0.865 | 0.827 | 0.895 |
| metal_nut | 0.643 | 0.467 | 0.565 | 0.910 | 0.883 | 0.948 | 0.436 | 0.272 | 0.443 | 0.851 | 0.821 | 0.922 | 0.891 | 0.872 | 0.948 | 0.870 | 0.848 | 0.930 |
| pill | 0.439 | 0.291 | 0.513 | 0.476 | 0.335 | 0.567 | 0.388 | 0.194 | 0.460 | 0.467 | 0.286 | 0.527 | 0.461 | 0.315 | 0.580 | 0.694 | 0.592 | 0.747 |
| screw | 0.399 | 0.265 | 0.488 | 0.638 | 0.569 | 0.756 | 0.594 | 0.498 | 0.719 | 0.615 | 0.551 | 0.725 | 0.640 | 0.616 | 0.769 | 0.742 | 0.698 | 0.800 |
| tile | 0.885 | 0.850 | 0.940 | 0.927 | 0.912 | 0.966 | 0.523 | 0.375 | 0.598 | 0.757 | 0.711 | 0.795 | 1.000 | 1.000 | 1.000 | 0.98 | 0.976 | 0.992 |
| toothbrush | 0.368 | 0.259 | 0.762 | 0.271 | 0.084 | 0.667 | 0.398 | 0.313 | 0.786 | 0.316 | 0.164 | 0.714 | 0.271 | 0.084 | 0.667 | 0.508 | 0.499 | 0.857 |
| transistor | 0.531 | 0.421 | 0.620 | 0.642 | 0.693 | 0.760 | 0.439 | 0.462 | 0.650 | 0.477 | 0.292 | 0.500 | 0.716 | 0.743 | 0.820 | 0.577 | 0.523 | 0.700 |
| wood | 0.743 | 0.672 | 0.868 | 0.782 | 0.644 | 0.868 | 0.375 | 0.196 | 0.574 | 0.750 | 0.651 | 0.868 | 0.850 | 0.790 | 0.927 | 0.816 | 0.756 | 0.912 |
| zipper | 0.526 | 0.417 | 0.615 | 0.583 | 0.518 | 0.652 | 0.455 | 0.291 | 0.548 | 0.608 | 0.515 | 0.689 | 0.639 | 0.552 | 0.659 | 0.726 | 0.667 | 0.756 |
| Mean | 0.613 | 0.526 | 0.712 | 0.670 | 0.601 | 0.769 | 0.516 | 0.394 | 0.641 | 0.631 | 0.542 | 0.721 | 0.675 | 0.609 | 0.769 | 0.736 | 0.674 | 0.805 |

Table 17. Detailed quantitative results on the MVTec AD dataset.

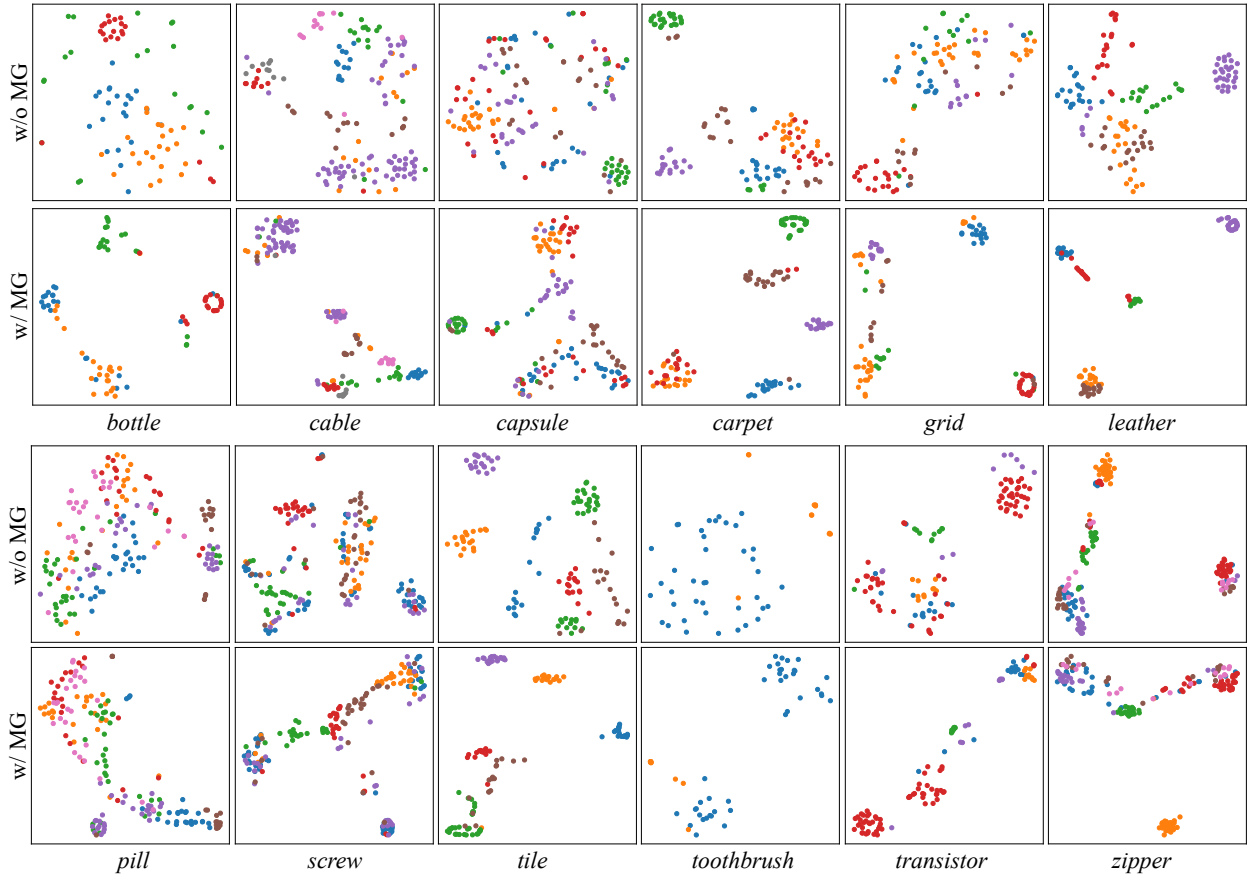


Figure 14. T-SNE visualization of sub-images on the MVtec AD dataset. The different colors of dots represent their anomaly classes.

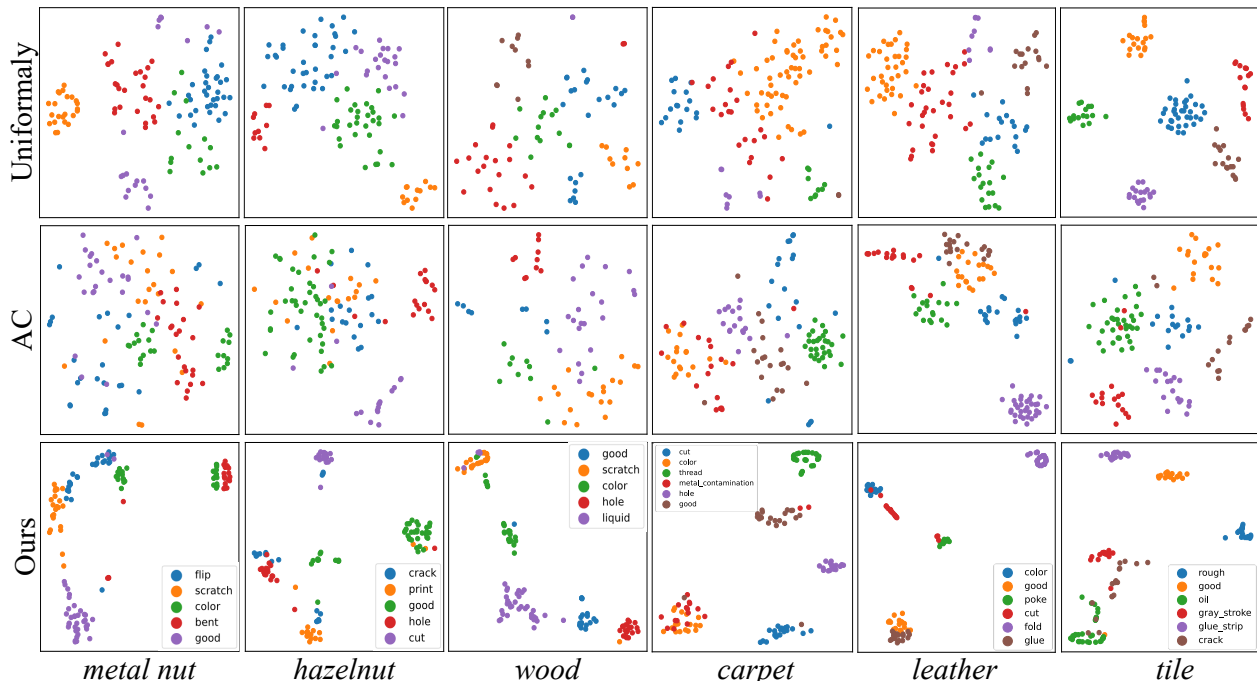


Figure 15. Qualitative comparisons with different clustering methods by t-SNE visualization.

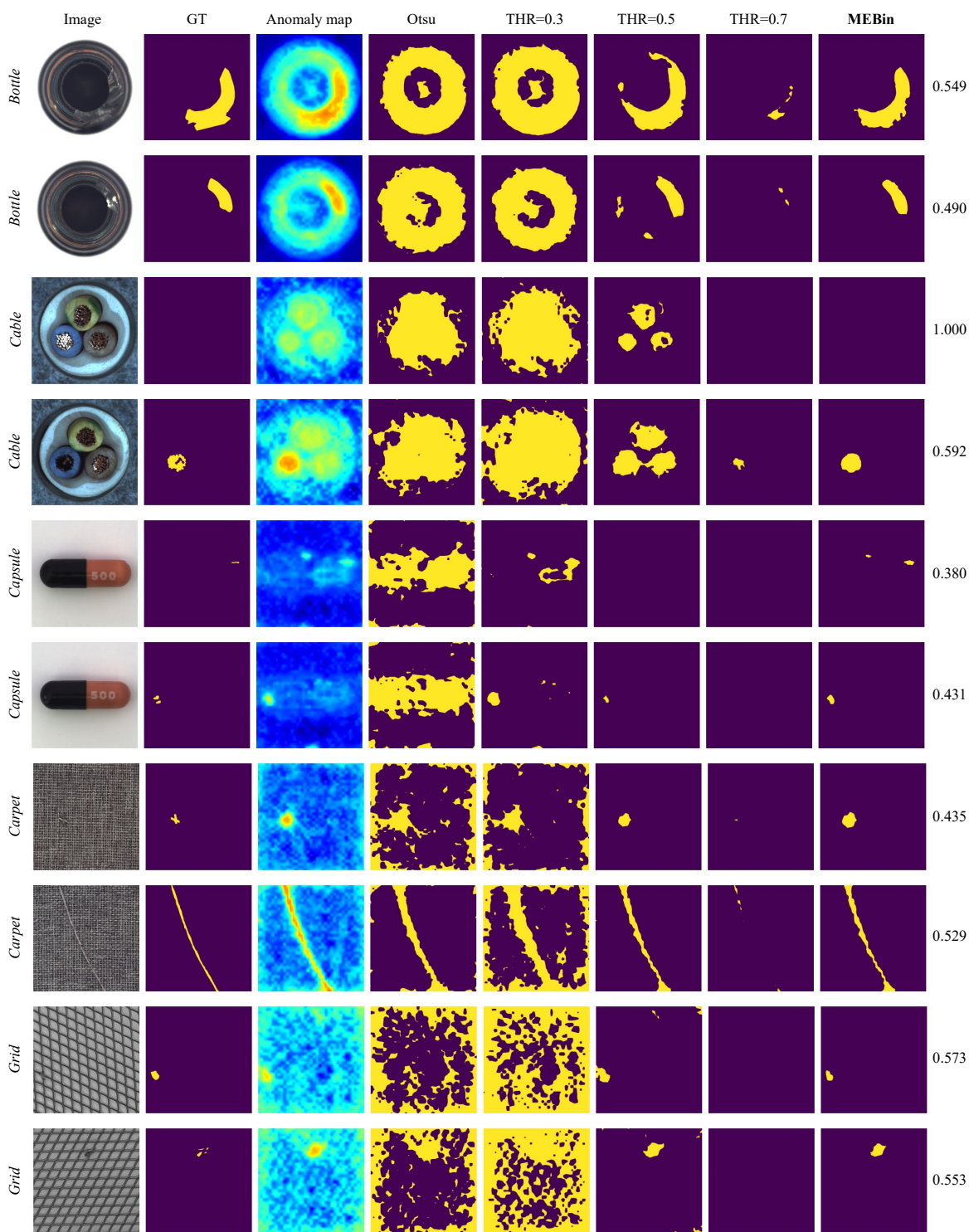


Figure 16. **Binarization results of MEBin on the MVTec AD dataset.** We show for each category: RGB image, ground truth, anomaly map, binary map of Otsu method, binary map of fixed threshold 0.3, binary map of fixed threshold 0.5, binary map of fixed threshold 0.7, and binary map of our MEBin. We report the optimal threshold searched by our MEBin in the last column.

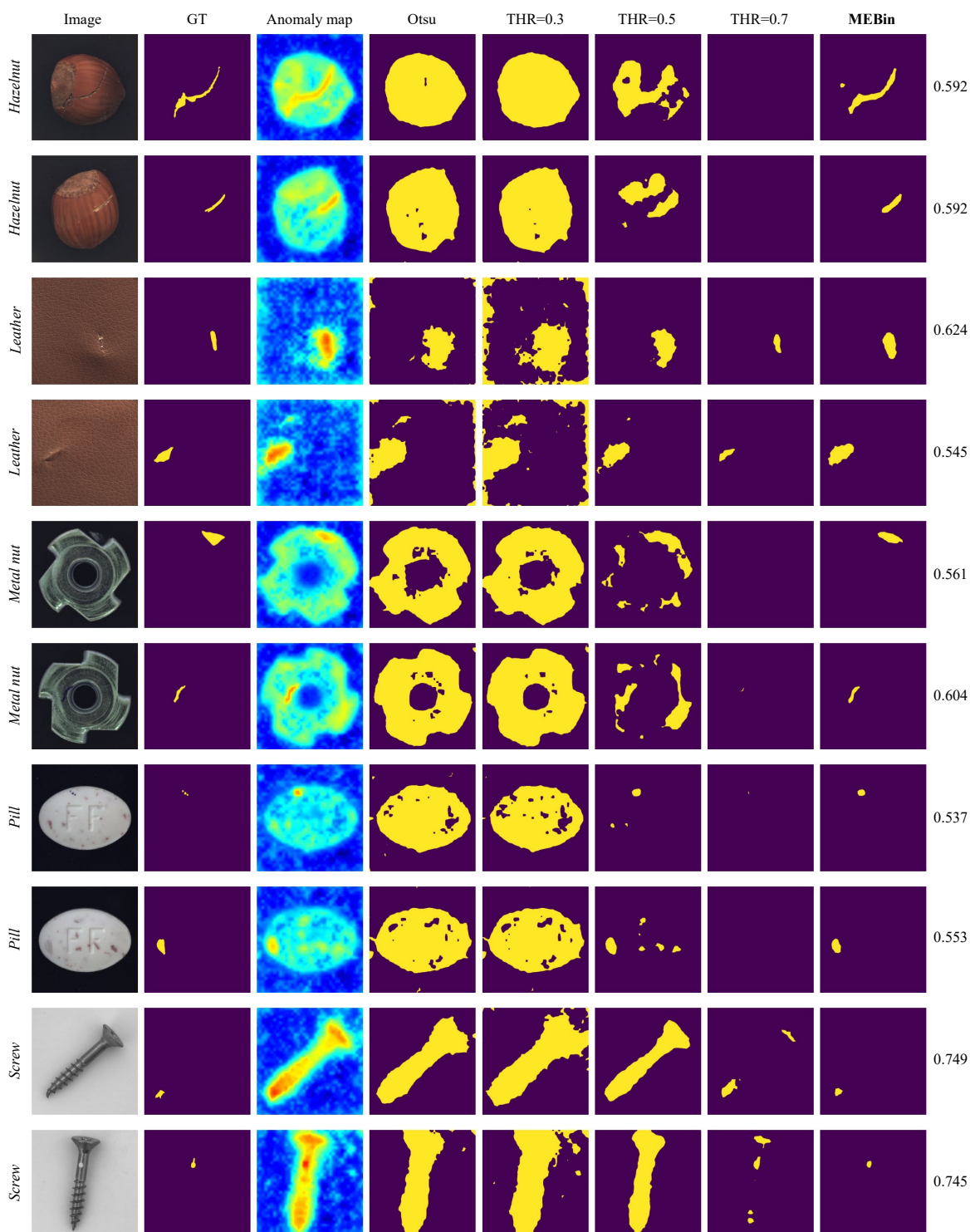


Figure 17. **Binarization results of MEBin on the MVTec AD dataset.** We show for each category: RGB image, ground truth, anomaly map, binary map of Otsu method, binary map of fixed threshold 0.3, binary map of fixed threshold 0.5, binary map of fixed threshold 0.7, and binary map of our MEBin. We report the optimal threshold searched by our MEBin in the last column.

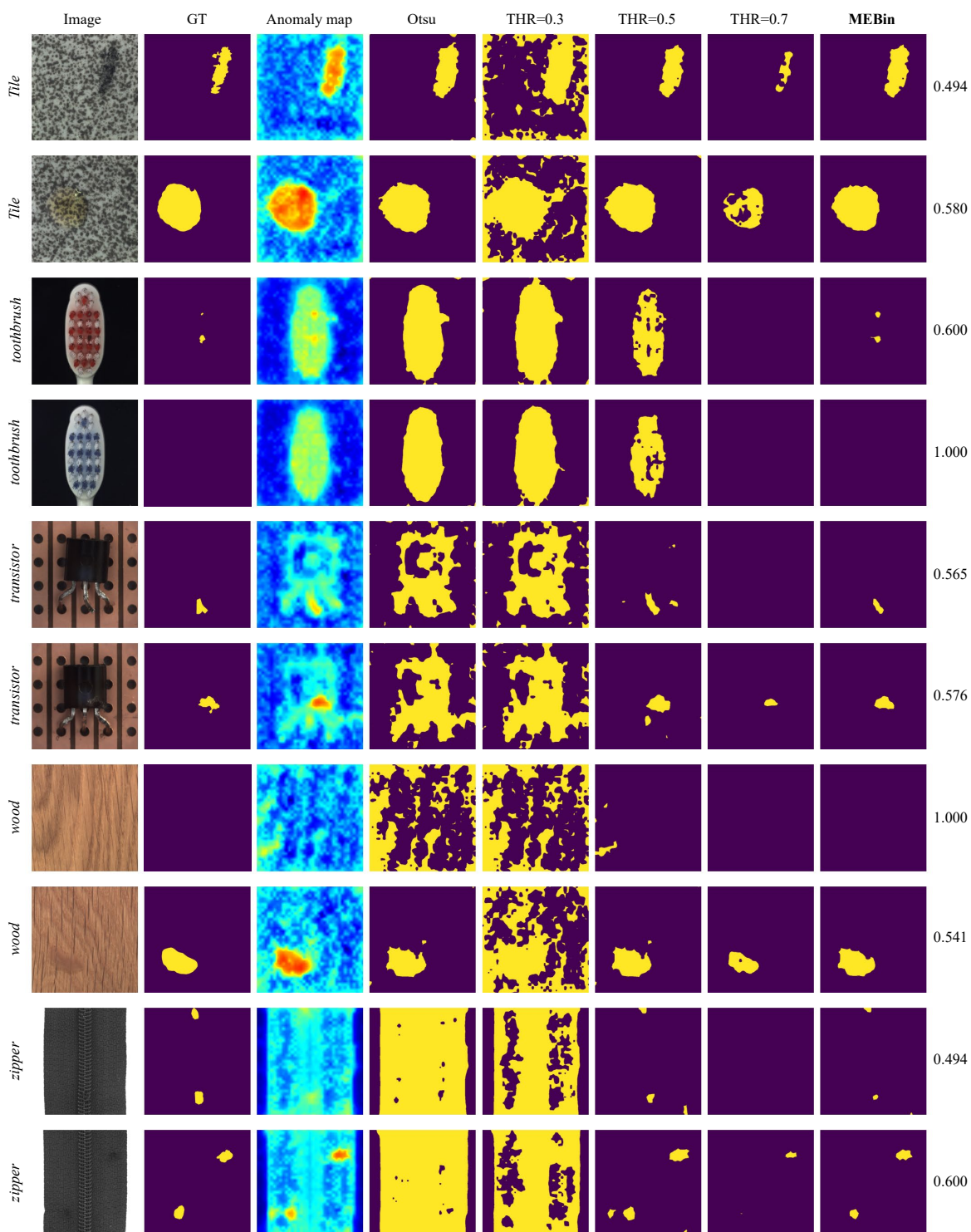


Figure 18. **Binarization results of MEBin on the MVTec AD dataset.** We show for each category: RGB image, ground truth, anomaly map, binary map of Otsu method, binary map of fixed threshold 0.3, binary map of fixed threshold 0.5, binary map of fixed threshold 0.7, and binary map of our MEBin. We report the optimal threshold searched by our MEBin in the last column.

References

- [60] Jaehyeok Bae, Jae-Han Lee, and Seyun Kim. Pni: industrial anomaly detection using position and neighborhood information. In *IEEE/CVF International Conference on Computer Vision (ICCV)*, 2023.
- [61] Kilian Batzner, Lars Heckler, and Rebecca König. Efficientad: Accurate visual anomaly detection at millisecond-level latencies. In *IEEE/CVF Winter Conference on Applications of Computer Vision (WACV)*, 2024.
- [62] Paul Bergmann, Michael Fauser, David Sattlegger, and Carsten Steger. Mvtec ad—a comprehensive real-world dataset for unsupervised anomaly detection. In *IEEE/CVF Conference on Computer Vision and Pattern Recognition (CVPR)*, 2019.
- [63] Léon Bottou. Large-scale machine learning with stochastic gradient descent. In *International Conference on Computational Statistics (COMPSTAT)*, 2010.
- [64] Mathilde Caron, Ishan Misra, Julien Mairal, Priya Goyal, Piotr Bojanowski, and Armand Joulin. Unsupervised learning of visual features by contrasting cluster assignments. *Advances in Neural Information Processing Systems (NeurIPS)*, 2020.
- [65] Mathilde Caron, Hugo Touvron, Ishan Misra, Hervé Jégou, Julien Mairal, Piotr Bojanowski, and Armand Joulin. Emerging properties in self-supervised vision transformers. In *IEEE/CVF International Conference on Computer Vision (ICCV)*, 2021.
- [66] Ekin D Cubuk, Barret Zoph, Jonathon Shlens, and Quoc V Le. Randaugment: Practical automated data augmentation with a reduced search space. In *IEEE/CVF Conference on Computer Vision and Pattern Recognition Workshop (CVPR Workshop)*, 2020.
- [67] Alexey Dosovitskiy, Lucas Beyer, Alexander Kolesnikov, Dirk Weissenborn, Xiaohua Zhai, Thomas Unterthiner, Mostafa Dehghani, Matthias Minderer, Georg Heigold, Sylvain Gelly, et al. An image is worth 16x16 words: Transformers for image recognition at scale. In *International Conference on Learning Representations (ICLR)*, 2021.
- [68] Enrico Fini, Enver Sangineto, Stéphane Lathuilière, Zhun Zhong, Moin Nabi, and Elisa Ricci. A unified objective for novel class discovery. In *IEEE/CVF International Conference on Computer Vision (ICCV)*, 2021.
- [69] Jean-Bastien Grill, Florian Strub, Florent Altché, Corentin Tallec, Pierre Richemond, Elena Buchatskaya, Carl Doersch, Bernardo Avila Pires, Zhaohan Guo, Mohammad Gheshlaghi Azar, et al. Bootstrap your own latent—a new approach to self-supervised learning. *Advances in Neural Information Processing Systems (NeurIPS)*, 2020.
- [70] Yibin Huang, Congying Qiu, and Kui Yuan. Surface defect saliency of magnetic tile. *The Visual Computer*, 36(1):85–96, 2020.
- [71] Yujin Lee, Harin Lim, Seoyoon Jang, and Hyunsoo Yoon. Uniformly: Towards task-agnostic unified framework for visual anomaly detection. *arXiv preprint arXiv:2307.12540*, 2023.
- [72] Hanxi Li, Jianfei Hu, Bo Li, Hao Chen, Yongbin Zheng, and Chunhua Shen. Target before shooting: Accurate anomaly detection and localization under one millisecond via cascade patch retrieval. *IEEE Transactions on Image Processing (TIP)*, 33:5606–5621, 2024.
- [73] Xurui Li, Ziming Huang, Feng Xue, and Yu Zhou. Musc: Zero-shot industrial anomaly classification and segmentation with mutual scoring of the unlabeled images. In *International Conference on Learning Representations (ICLR)*, 2024.
- [74] Nobuyuki Otsu. A threshold selection method from gray-level histograms. *IEEE Transactions on Systems, Man, and Cybernetics (TSMC)*, 9(1):62–66, 1979.
- [75] Karsten Roth, Latha Pemula, Joaquin Zepeda, Bernhard Schölkopf, Thomas Brox, and Peter Gehler. Towards total recall in industrial anomaly detection. In *IEEE/CVF Conference on Computer Vision and Pattern Recognition (CVPR)*, 2022.
- [76] Kihyuk Sohn, Jinsung Yoon, Chun-Liang Li, Chen-Yu Lee, and Tomas Pfister. Anomaly clustering: Grouping images into coherent clusters of anomaly types. In *IEEE/CVF Winter Conference on Applications of Computer Vision (WACV)*, 2023.
- [77] Tran Dinh Tien, Anh Tuan Nguyen, Nguyen Hoang Tran, Ta Duc Huy, Soan Duong, Chanh D Tr Nguyen, and Steven QH Truong. Revisiting reverse distillation for anomaly detection. In *IEEE/CVF Conference on Computer Vision and Pattern Recognition (CVPR)*, 2023.
- [78] Muli Yang, Liancheng Wang, Cheng Deng, and Hanwang Zhang. Bootstrap your own prior: Towards distribution-agnostic novel class discovery. In *IEEE/CVF Conference on Computer Vision and Pattern Recognition (CVPR)*, 2023.